Draft version November 22, 2021
Typeset using LaTeX default style in AASTeX63

The extended field-aligned suprathermal proton beam and long-lasting trapped energetic particle population observed upstream of a transient interplanetary shock

D. Lario,[1] I. G. Richardson,[2,1] L. B. Wilson III,[1] L. Berger,[3] L. K. Jian,[1] and D. Trotta[4]

[1] Heliophysics Science Division, NASA Goddard Space Flight Center, Greenbelt, MD 20771, USA
[2] Department of Astronomy, University of Maryland, College Park, MD 20742, USA
[3] Institut für Experimentelle und Angewandte Physik (IEAP), Christian-Albrechts-Universitt zu Kiel, 24118 Kiel, Germany
[4] Dipartimento di Fisica, Università della Calabria, I-87036 Cosenza, Italy

(Received; Revised; Accepted)

Submitted to ApJ

ABSTRACT

The properties of the suprathermal particle distributions observed upstream of interplanetary shocks depend not only on the properties of the shocks but also on the transport conditions encountered by the particles as they propagate away from the shocks. The confinement of particles in close proximity to the shocks, as well as particle scattering processes during propagation to the spacecraft, lead to the common observation of upstream diffuse particle distributions. We present observations of a rare extended anisotropic low-energy ($\lesssim$30 keV) proton beam together with a trapped $\gtrsim$500 keV proton population observed in association with the arrival of an oblique interplanetary shock at the ACE, *Wind* and IMP-8 spacecraft on 2001 January 31. Continuous injection of particles by the traveling shock into a smooth radial magnetic field region formed in the tail of a modest high-speed solar wind stream produced an extended foreshock region of energetic particles. The absence of enhanced magnetic field fluctuations upstream of the shock results in the observation of a prolonged anisotropic field-aligned beam of $\lesssim$30 keV protons as well as a population of higher-energy ($\gtrsim$500 keV) protons with small pitch-angle cosine ($\mu\sim0$) extending far from the shock.

Keywords: Solar wind, Shock waves; Magnetic fields, Interplanetary; Energetic particles, Acceleration

1. INTRODUCTION

Energetic particle intensity enhancements associated with the passage of traveling interplanetary shocks past Earth are known as Energetic Storm Particle (ESP) events due to their concurrence with geomagnetic storms that commence at the same shock (Bryant et al. 1962). ESP events exhibit a large variety of energetic particle intensity-time profiles (e.g., van Nes et al. 1984; Tsurutani & Lin 1985; Wenzel et al. 1985; Kallenrode 1995; Lario et al. 2005). In general, the spatial distribution of energetic particles observed in ESP events depends on the conditions for particle acceleration at the shock, for particle escape from the vicinity of the shock, and for particle transport between the shock and the observing spacecraft (e.g., Sanderson et al. 1985; van Nes et al. 1985). Ion distributions in ESP events may consist of both particles locally accelerated at the time of the shock passage and particles previously accelerated at the shock that remain confined in the vicinity of the shock by either scattering processes undergone by the particles as they interact with the pre-existing or self-amplified turbulent medium or by the effects produced by intervening solar wind structures (e.g., Gosling 1983; Lario & Decker 2002; Lee 2005; Shen et al. 2008).

Because of the characteristics of spacecraft instrumentation, a distinction is often made between energetic ions at energies $\gtrsim$50 keV observed by “energetic particle” instruments and “suprathermal” ions, usually detected by solar wind

Corresponding author: D. Lario
david.larioloyo@nasa.gov

plasma instruments, with energies $\lesssim$30 keV but higher than those of the thermal population whose energy spectrum can be described by a quasi-Gaussian distribution. In this paper we will make this distinction to refer to energetic particles (i.e., $\gtrsim$50 keV), suprathermal particles (i.e., $\lesssim$30 keV), or thermal solar wind particles.

By analogy with the particle distributions observed in the Earth's bow shock (e.g., Thomsen 1985; Wilson 2016, and references therein), low-energy ($\lesssim$30 keV) particle distributions observed upstream of traveling interplanetary (IP) shocks can be described in terms of: (1) Upstream field-aligned beams, characterized by a relatively collimated flow away from the shock along the magnetic field and by a sharp energy peak that rarely exceeds more than ∼10 keV in Earth's foreshock; (2) Diffuse distributions, characterized by broad, nearly isotropic angular distributions that often exhibit flat energy spectra in phase space density units up to several 10s of keV but that can extend to high energies up to ∼300 keV in the case of Earth's bow shock, whereas in the case of traveling IP shocks they can extend up to several MeV; (3) Intermediate distributions, similar to field-aligned beams but which exhibit a large spread in pitch-angle and are thought to result from pitch-angle scattering of gyrating ions; (4) Gyrating ion distributions which are symmetric about the quasi-static magnetic field direction and are produced near the quasi-parallel region of the Earth's bow shock by specular reflection; and (5) Gyrophase-bunched ions which are symmetric about the magnetic field direction but tend to form at larger distances from the bow shock through wave-particle interactions. The first three types are all nearly gyrotropic and are distinguished primarily by their pitch-angle distributions (PADs) and range of energies, whereas the level of gyrotropy and distance from the bow shock where they are observed distinguish gyrating and gyrophase-bunched ions. Examples of these ion distributions can be found in Figure 16.4 of Wilson (2016).

At energies $\gtrsim$50 keV, the ion distributions observed in association with the passage of IP shocks may include the following: (1) A slow, quasi-exponential increase of the ion intensity extending several hours upstream of the shock, followed by a nearly constant intensity downstream, with a moderate upstream flow of particles away from the shock and isotropic distributions in the downstream medium that are consistent with particles being accelerated at the shock by the diffusive shock acceleration (DSA) mechanism (Lee 1983). (2) A spike of a few ($\lesssim$10) minutes duration at or near the shock, with large upstream anisotropies and moderate downstream anisotropy and indications of protons gyrating about the magnetic field with pitch angles around 90° consistent with particle acceleration by the shock drift acceleration (SDA) mechanism (Decker 1983). (3) Isotropic step-like, post-shock intensity increases produced when small-gyroradii particles get coupled to the downstream solar wind plasma (Tsurutani & Lin 1985). And (4) ion distributions that, depending on energy, are unchanged by the passage of the shock. Examples of these ESP energetic particle signatures can be found elsewhere (e.g., Sanderson et al. 1985; Tsurutani & Lin 1985; Kallenrode 1995; Lario et al. 2003, 2005).

During the passage of IP shocks, ion intensities at energies $\lesssim$30 keV very often exhibit a significant increase at the time of the shock passage and stay elevated for a long distance downstream of the shock. However, such ions are only rarely detectable upstream of the shock (e.g., Gosling et al. 1978a, 1984; Lario et al. 2019). Shock geometry, the ability of the suprathermal particles to escape from the vicinity of the shock, and instrument capabilities, all influence the detectability of upstream suprathermal ions (Lario et al. 2019). For those IP shocks with ion distributions that can be detected by current instruments, the $\lesssim$30 keV ion distributions commonly resemble those of diffuse events, whereas observations of field-aligned beams, gyrating ions and reflected ions upstream of IP shocks are very rare (e.g., Gosling 1983; Gosling et al. 1984; Tokar et al. 2000; Kajdič et al. 2017; Cohen et al. 2019; Yang et al. 2020). Gosling (1983) suggested that a spacecraft establishes magnetic connection with IP shocks through field lines that remain connected to the large-scale structure of the traveling shock for an extended time, resulting in an ESP event where the $\lesssim$30 keV ion distributions consist not only of particles locally accelerated at the arrival of the shock but also of particles accelerated earlier by the shock that remain confined close to the shock. Particles leaving the shock may encounter, and be scattered by, magnetic perturbations generated self-consistently further upstream, resulting in the diffuse distributions that are usually observed in ESP events (Gosling 1983; Wilson et al. 2009; Blanco-Cano et al. 2016). Another key ingredient for particles to be efficiently scattered in the shock upstream is the presence of pre-existing fluctuations, due to the ambient turbulence in which shocks propagate (e.g., Guo et al. 2021; Trotta et al. 2021).

Here we report measurements of an unusual ESP event showing a macro-scale, long-lasting, field-aligned, proton beam upstream of an oblique shock at low-energies ($\lesssim$30 keV). This event also shows a population of $\gtrsim$500 keV protons with angular distributions peaking at ∼90° pitch angles trapped between the shock and the tail of a preceding modest high-speed solar wind stream. What makes this event unusual is the extended region upstream of the shock for which both populations were observed. This region was characterized by a smooth magnetic field with very few

Table 1. Spacecraft locations and interplanetary shock parameters at ACE and *Wind*

Catalog	r_n	r_b	V_s	M_{ms}	θ_{Bn}	$\vec{n}$
ACE shock at 07:22 UT (day 31.307)				(x_{GSE}=241.19, y_{GSE}=-13.86, z_{GSE}=24.35 R$_E$)		
ipshocks.fi[a]	3.2±0.7	2.2±0.1	387±29	1.5±0.2	51±9	(-0.70±0.08, 0.70±0.08, 0.16±0.11)
CfA shock list[b]	3.9±0.5	2.2±0.4	410±11	1.5±0.1	44±3	(-0.80±0.01, 0.55±0.01, 0.23±0.22)
IMP-8 shock at 08:09 UT (day 31.339)				(x_{GSE}=8.00, y_{GSE}=30.56, z_{GSE}=-21.64 R$_E$)		
Wind shock at 08:35 UT (day 31.358)				(x_{GSE}=-20.91, y_{GSE}=196.1, z_{GSE}=-12.88 R$_E$)		
ipshocks.fi[a]	2.7±0.6	2.6±0.2	431±29	2.1±0.4	54±8	(-0.81±0.06, 0.29±0.15, 0.51±0.11)
CfA shock list[b]	2.3±0.2	2.6±0.6	485±16	3.5±0.2	45±4	(-0.84±0.02, 0.44±0.03, 0.33±0.32)

[a] ipshocks.fi/ (Kilpua et al. 2015)

[b] www.cfa.harvard.edu/shocks/

field fluctuations, suggesting that conditions were favorable for nearly scatter-free particle transport. We suggest that the observation of a long-lasting, field-aligned beam of low-energy particles upstream of transient IP shocks requires the presence of a magnetically quiet region upstream of the shock, and that the formation of a long-lasting trapped high-energy particle population additionally requires the presence of magnetic field disturbances far from the shock that allow the escape of high-energy particles with large pitch-angle cosine ($|\mu|\sim1$) but confine particles with small pitch-angle cosine ($\mu\sim0$).

2. OBSERVATIONS

A relatively strong interplanetary shock was observed by the magnetic field experiment (MAG; Smith et al. 1998) and the Solar Wind Electron, Proton, and Alpha Monitor (SWEPAM; McComas et al. 1998) on board the *Advanced Composition Explorer* (ACE) at 07:22 UT on day 31 (January 31) of 2001. In units of fractional day of the year, the shock arrived at ACE at day 31.307. The same IP shock was observed by the Magnetic Field Investigation (MFI; Lepping et al. 1995) and the Solar Wind Experiment (SWE; Ogilvie et al. 1995) on board the *Wind* spacecraft at 08:35 UT on the same day (day 31.358). The Solar Plasma Faraday cup experiment (PLS; Bellomo & Mavretic 1978) on board the *Interplanetary Monitoring Platform*-8 (IMP-8) detected an abrupt increase in solar wind density, speed and temperature at 08:09 UT (day 31.339), that most likely was associated with the passage of the shock by this spacecraft. Unfortunately, the lack of magnetic field data from IMP-8 (whose magnetometer failed in June 2000) prevents us from fully characterizing the shock at this spacecraft. Table 1 lists the locations of these three spacecraft in Geocentric Solar Ecliptic (GSE) coordinates at the time of the respective shock passages.

Table 1 provides also the main shock parameters at ACE and *Wind* as listed in the Database of Heliospheric Shock Waves generated by the University of Helsinki at ipshocks.fi (Kilpua et al. 2015), and the Harvard-Smithsonian Center for Astrophysics (CfA) Interplanetary Shock Database at www.cfa.harvard.edu/shocks/ using the method RH08 to solve the set of Rankine-Hugoniot (RH) continuity equations across the shock as described in Szabo (1994) and Koval & Szabo (2008). In particular, the RH08 method is a nonlinear least-squares fitting technique that uses eight equations derived from the RH mass flux conservation equation, the conservation equation for the tangential components of the momentum flux, the continuity equation for the tangential electric field, and the continuity of the normal component of the magnetic field (see Vinas & Scudder (1986) and the supplemental material in Wilson et al. (2017) for details). Specifically, Table 1 lists the density compression ratio r_n, the magnetic field compression ratio r_b, the shock speed in the spacecraft frame of reference V_s, the fast magnetosonic Mach number M_{ms}, the angle between the normal to the shock and the upstream magnetic field θ_{Bn}, and the normal to the shock $\vec{n}$ in GSE coordinates, as obtained from solving the RH equations using either ACE (top) or *Wind* (bottom) data. Within the error bars, the shock parameters from both databases seem consistent, even when different approaches were used to select the time intervals representative of the upstream and downstream media and to compute the shock parameters. There are only slight differences between the parameters of the shock at ACE and at *Wind*. Whereas the shock at ACE was relatively strong $r_n>3$ and its magnetosonic Mach number was a modest $M_{ms}\sim1.5$, the shock at *Wind* was weaker $r_n\sim2.5$, but with a larger magnetosonic Mach number $M_{ms}>2$, even though the shock was oblique $\theta_{Bn}\gtrsim45°$ at both spacecraft. Small differences between shock parameters at ACE and *Wind* should be expected (e.g., Szabo et al. 2001) since the two spacecraft intercepted the shock at different times and at different heliospheric locations.

2.1. *Solar energetic particle observations*

The most likely solar origin of the shock observed by the three spacecraft on 2001 January 31 was a halo coronal mass ejection (CME) first seen by the C2 coronagraph of the Large Angle and Spectrometric Coronagraph (LASCO) on board the *Solar and Heliospheric Observatory* (SOHO) (Brueckner et al. 1995) at 15:54 UT on 2001 January 28 propagating with a plane-of-sky speed of 916 km s^{-1} as reported in the Coordinated Data Analysis Web (CDAW)[1] CME catalog. This CME was temporally associated with a M1.5/1N solar flare from NOAA Active Region 9313 at S04W59 with 1-8 Å X-ray emission starting at 15:40 UT, peaking at 16:00 UT and ending at 16:24 UT on 2001 January 28. The absence of signatures suggestive of an interplanetary coronal mass ejection following the passage of this IP shock by ACE, IMP-8 and *Wind* (Richardson & Cane 2010a) is consistent with an encounter with the flank of the shock from this western solar event. The solar eruption generated a solar energetic particle event (SEP) observed by the energetic particle instruments on board the three spacecraft. The following sections describe these SEP observations and the influence of the IP structures preceding the shock on the energetic particles.

2.1.1. *ACE solar energetic particle observations*

Figure 1 shows a collection of data from the ACE spacecraft during the associated SEP event. Figure 1a shows spin-averaged ion intensities at energies from 47 keV to 4.8 MeV measured in eight energy channels of the LEMS120 telescope of the Electron, Proton, and Alpha Monitor (EPAM) on board ACE (Gold et al. 1998). The ACE/EPAM/LEMS120 telescope does not distinguish among different ion species, and we assume that ion intensities in Figure 1a are dominated by the more abundant protons. Figures 1(b-d) show the solar wind proton (b) speed V_{sw}, (c) density N_p, and (d) temperature T_p measured by ACE/SWEPAM. Figures 1(f-j) show magnetic field data collected by ACE/MAG. In particular, Figure 1f shows the magnetic field magnitude B, and Figures 1g and 1h, the polar θ_{GSE} and azimuth ϕ_{GSE} angular magnetic field directions in GSE coordinates, respectively. Figure 1i shows the angle α_R formed between the magnetic field and the Sun-ACE radial direction. Figure 1j shows the root mean square (rms) of the magnetic field vector dBrms computed using high-resolution measurements of ACE/MAG (3 vectors per second) as $\left[\sum_{i=1}^{3} < (B_i - < B_i >)^2 >\right]^{1/2}$ where B_i is each component of the vector $\vec{B}$ and $<>$ is the average over 16 second intervals. Figure 1e shows the proton plasma beta β_p computed as the ratio of the proton thermal energy $N_p \kappa T_p$ to the magnetic energy $B^2/8\pi$. We have indicated by red shading those periods when $\beta_p<0.5$. The vertical arrow in Figure 1a indicates the onset of the soft X-ray solar flare associated with the origin of the SEP event. The vertical black solid line marks the time of the passage of the shock by ACE.

ACE/EPAM/LEMS120 ion intensities at $\gtrsim$2 MeV started to increase above the pre-event background shortly ($\lesssim$6 h) after the occurrence of the solar flare. Energetic ions arrived at ACE when the spacecraft was immersed in a region of elevated magnetic field intensity and solar wind density with $\beta_p<0.5$ observed by ACE between day ∼28.8 and day ∼29.7. This region is most likely a stream interaction region (SIR) (Richardson 2018) resulting from the interaction between the preceding slow (∼300 km s^{-1}) solar wind and the following faster solar wind. The time of maximum solar wind speed (∼500 km s^{-1}) at day 29.75, also associated with decreases in density and magnetic field intensity, marks the trailing edge of the SIR. Particle intensities at energies $\gtrsim$300 keV abruptly increased at day 29.2 coinciding with a sharp decrease of N_p and increase of T_p, and changes in the solar wind ion charge states (not shown here) observed by the Solar Wind Ion Composition Spectrometer (SWICS; Gloeckler et al. 1998) on board ACE . These are typical signatures of the stream interface (SI) within an SIR (Burlaga 1974; Gosling et al. 1978b; Forsyth & Marsch 1999). We indicate the passage of this SI by a vertical pink line in Figure 1. After this sudden energetic particle intensity increase, all particle intensities below $\lesssim$2 MeV converged as they gradually increased with time. We indicate this period of similar intensity levels at energies $\lesssim$2 MeV by the tilted hatched rectangle in Figure 1a. Note that the 47-68 keV ion intensities (red trace in Figure 1a) only acquired this common intensity value around day ∼29.75 due to the elevated pre-event background and possible contamination by higher-energy particles that can occur in this lowest energy channel early in SEP events (e.g., Marhavilas et al. 2015). The rising phase of the SEP event at energies $\lesssim$2 MeV was therefore characterized by a flat energy spectrum (similar examples can be found in Lario et al. 2018). The ion intensity-time profiles then departed from the flat-spectrum intensity level at a time that is ordered by energy – the higher the energy, the earlier the ion intensities separated from the common flat-spectrum intensity level. At energies

---

[1] cdaw.gsfc.nasa.gov/CME_list/

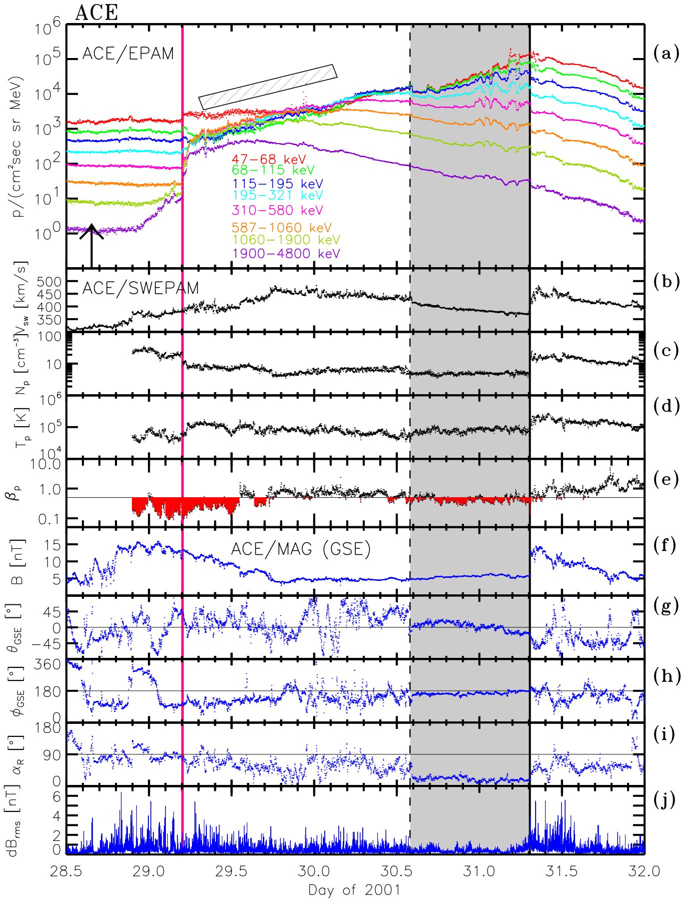

Figure 1. From top to bottom: (a) 96-second averages of spin-averaged ion intensities measured in eight differential energy channels of the telescope LEMS120 of the EPAM instrument on board ACE; 64-second averages of the solar wind proton (b) speed V_{sw}, (c) density N_p, and (d) temperature T_p as measured by the ACE/SWEPAM; 64-second averages of the (e) proton plasma β_p; 64-second averages of the magnetic field (f) magnitude B, (g) polar θ_{GSE}, and (h) azimuth ϕ_{GSE} angular directions in GSE coordinates, and (i) the angle α_R between the magnetic field and the Sun-ACE radial direction as measured by ACE/MAG; (j) the rms value of the magnetic field vector dBrms computed as described in the text. The pink vertical line identifies the passage of the stream interface (SI), the black solid vertical line the passage of the IP shock and the dashed vertical line marks the onset of an upstream smooth-field low-β_p region. The vertical arrow in panel (a) indicates the onset of the soft X-ray parent solar flare. The tilted hatched bar in panel (a) indicates the period with nearly flat energy spectrum at energies $\lesssim$2 MeV.

below ~300 keV ion intensities kept increasing until the arrival of the shock, with the lower energies displaying a higher increase. The ion intensity-time profiles at energies $\gtrsim$2 MeV did not reach the common flat-spectrum intensity level, but reached a maximum around day ~29.5 and then gradually decreased.

Prior to the arrival of the shock, ACE observed a region of at least ~16 hours characterized by a very smooth magnetic field closely aligned with the radial direction ($\alpha_R \lesssim 25°$), a decreasing solar wind speed V_{sw} and $\beta_p \lesssim 0.5$ in the trailing part of the high speed stream. The dashed black vertical line and gray shaded bar in Figure 1 indicate the start time and duration of this region (ending at the shock) at ACE, respectively. Magnetic field fluctuations within this region were much smaller than in either the preceding solar wind or in the downstream region of the shock (Figure 1j). Magnetic field directions that tend to be more radial than the nominal Parker spiral magnetic field direction have been regularly observed during periods when the solar wind speed decreases (e.g., Lario & Roelof 2010, and references therein), and the trailing edges of high-speed streams at 1 au also exhibit a decay in the amplitude of Alfvénic fluctuations (e.g., Borovsky & Denton 2016; Carnevale et al. 2021). Therefore, we suggest that this quiet radial magnetic field region is a similar example, lying in the tail of the preceding modest high-speed solar wind stream. Shock-accelerated particles escaping from the vicinity of the shock and reaching the spacecraft before shock arrival would most likely have propagated through this region.

Anisotropy observations are also valuable for interpreting particle events. However, the spin axis of ACE points toward the Sun within ±20° (i.e., close to the radial direction), and therefore, the range of pitch-angles scanned by each of the EPAM telescopes when the magnetic field orientation is close to radial is very limited (see Figure 2 of Gold et al. 1998). In addition, the measurement of anisotropies by combining different ACE/EPAM telescopes is restricted because the energy ranges of these telescopes are not perfectly matched. Anisotropy observations are then presented for the two other spacecraft (IMP-8 and *Wind*).

2.1.2. *IMP-8 solar energetic particle observations*

The IMP-8 spacecraft also observed the SEP event commencing on 2001 January 28. Figure 2 shows particle observations collected by IMP-8 from day 28.5 to day 32 of 2001. At this time, IMP-8, in Earth orbit, was in the solar wind and approaching the dusk flank of Earth's bow shock (Table 1). Figures 2a-d show particle data from the Goddard Medium Energy (GME) instrument on IMP-8 (McGuire et al. 1986). Because of the lack of IMP-8 magnetic field data and the noisy data from IMP-8/PLS, we again show in Figures 2e-i ACE magnetic field and plasma observations. In particular, Figure 2e shows the magnetic field intensity (black) and plasma density (red), Figure 2f the polar and Figure 2g azimuthal angles of the magnetic field in GSE coordinates, Figure 2h the solar wind temperature (black) and the "expected temperature" (red) (Richardson & Cane 1995), computed assuming the well-established correlation between V_{sw} and T_p for normal solar wind expansion, and Figure 2i the solar wind speed. Since the solar wind travel time from ACE to IMP-8 was <1 hour, this can be ignored in this overview plot. Note however that the arrival time of the shock at IMP-8 (vertical green line) was slightly later than at ACE (see Table 1). The gray shaded region corresponds to the interval of quiet, near radial magnetic field identified in Figure 1.

Figure 2d shows 30 minute averages of the proton intensity in selected GME energy channels ranging from 0.88-1.15 MeV to 63-81 MeV. These observations show even more clearly than the ACE data in Figure 1 the energy-dependence of the intensity time profiles during the onset of the SEP event. The higher energy ($\gtrsim$25 MeV) intensities rose promptly following the time of the flare (indicated by the black arrow in Figure 2d), then slowly decayed over the next ~3 days. The intensity at lower ($\lesssim$4 MeV) energies rose more slowly, with (as at ACE) an abrupt increase coincident with the passage of the SI (indicated by the vertical pink line in Figure 2). This suggests that the lower energy ions propagated to Earth more efficiently within the high speed stream than in the preceding slower solar wind whereas higher energy ions populated both slow and high-speed streams. There is little evidence of the passage of the shock on the declining particle intensities except for a very small brief enhancement close to the shock in the lowest energy channels shown.

Figures 2a-c summarize the particle anisotropies measured by IMP-8/GME. The results presented here are for 0.5-4 MeV/n protons and He ions measured by the GME Low Energy Detector (LED). IMP-8 rotated on an axis perpendicular to the ecliptic and particle counts from the LED telescope (with a field of view ±25° from the ecliptic) were accumulated in eight azimuthal sectors. Correction for the Compton-Getting effect (Ipavich 1974) has been applied in the count rates shown in Figure 2. The pie plots at the top of Figure 2 show representative examples of sectored particle counting rates plotted vs. instrument viewing direction with the Sun to the top of each plot. The counts are accumulated over a 15 minute interval starting at the time shown; the number of counts s^{-1} in the maximum count sector is also shown. The first pie plot (from early in the SEP event) shows a typical case of particles streaming away from the Sun with a distribution approximately centered on the magnetic field direction shown by the arrow (based on 1 minute OMNI data[2] during the data accumulation interval) and lying approximately along the outward Parker spiral direction. Figure 2a summarizes the sectored particle counting rates during the SEP event. It shows a sequence of third-order Fourier series fits in azimuth to the sectored count rates (to smooth the sectored data) for each 15 minute interval (Richardson & Reames 1993), normalized to the maximum intensity in that interval. The normalized intensities are plotted vs. instrument viewing direction in GSE coordinates. Black horizontal dashed lines indicate the directions parallel and anti-parallel to the measured local magnetic field direction (from OMNI). Thus, a particle flow away from (towards) the Sun along the nominal Parker spiral direction would be indicated by maximum intensities at around 315° (135°). Figure 2a clearly shows highly anisotropic, anti-solar flows that persisted for around a day after the solar event, after which the distribution became more isotropic (see also the second pie plot at the top of Figure 2). Figure 2b illustrates the direction-averaged sectored 0.5-4 MeV/n proton plus He counting rate, which again shows the large jump at the stream interface. The intensity enhancement in the vicinity of the shock (and predominantly upstream), is more evident here than in Figure 2d because of the lower energy threshold and the 15

---

[2] omniweb.gsfc.nasa.gov/html/omni_min_data.html

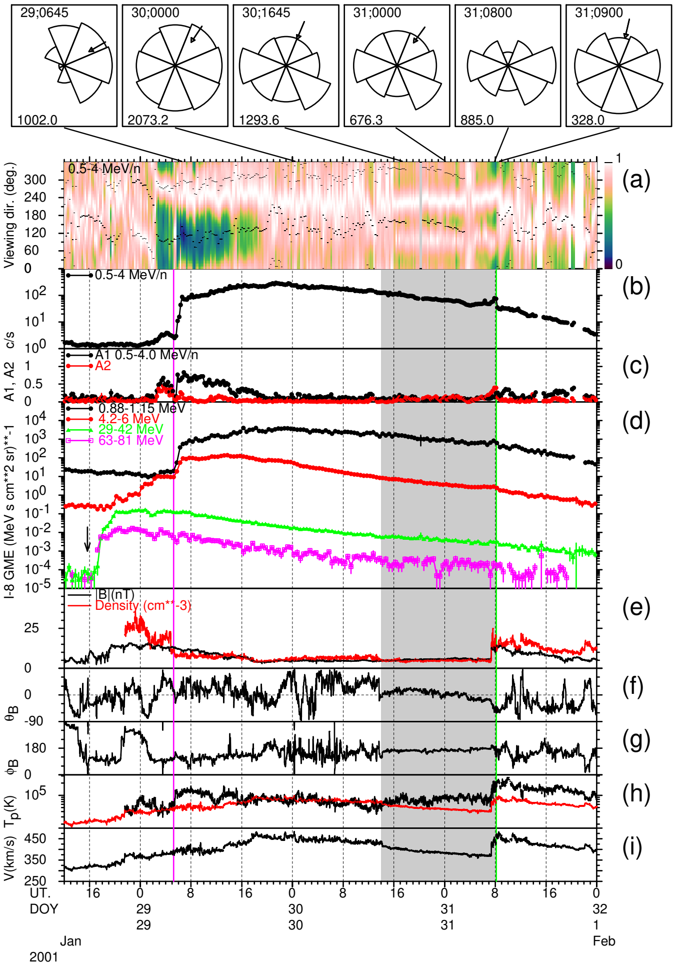

Figure 2. Summary of (a-d) IMP-8/GME particle observations during the 2001 January 28 SEP event and (e-i) ACE solar wind data. Top row: Pie plots of sectored 0.5–4 MeV/n proton plus He counting rates vs. instrument viewing direction in 15 minute intervals starting at the times indicated. The small arrow indicates the magnetic field direction (from the OMNI database). The counting rate (s^{-1}) in the maximum sector is also shown. (a) Normalized third-order Fourier fits to the sectored data plotted vs. instrument viewing direction (GSE coordinates). Particles streaming away from (toward) the Sun along a nominal Parker spiral magnetic field would be at directions ∼315 (∼135) deg. Black dashed lines indicate the directions parallel and anti-parallel to the locally observed magnetic field (from OMNI). (b) Average sectored counting rate for the 0.5-4 MeV/n anisotropy observations. (c) Amplitudes of the first and second Fourier components of the 0.5-4 MeV/n proton plus He sectored data. (d) Proton intensities from 0.88 MeV to 81.0 MeV separated in four energy channels. (e-i) ACE solar wind magnetic field and plasma data, specifically: (e) magnetic field intensity (black) and solar wind proton density (red); (f) magnetic field polar angle in GSE coordinates, (g) magnetic field azimuth angle in GSE coordinates; (h) solar wind proton temperature; and (i) solar wind proton speed. The time of the associated solar flare is indicated by the black arrow in panel (d). The arrival time of the shock at IMP-8 is shown by the vertical green line, while the gray shaded region indicates the interval of quiet radial field shown in Figure 1. The vertical pink line indicates the SI in the SIR on days 28-29 associated with an abrupt jump in the low-energy particle intensity. The unusual particle distributions, tending to peak close to ∼90° from the magnetic field direction in the quiet field region are evident in panel (a) and in the corresponding sector pie plots. The pancake distribution found close to shock passage is shown in the pie plot for 08:00 UT on January 31. The final pie plot shows sunward flows immediately after the shock.

minute, rather than 30 minute, averaging. Figure 2c gives the amplitudes of the first- (A1) and second- (A2) order Fourier components. Note for example the large A1 component during the interval of anti-solar streaming early in the SEP event.

Examining the angular distributions in Figure 2a, a striking feature is evident in the interval between ∼16 UT on 2001 January 30 (day 30.67) shortly after the start of the shaded region of quiet magnetic field, and the passage of the shock on day 31, where there are two persistent intensity peaks (bands of light shading) that tend to lie away from the magnetic field direction. The third and fourth pie plots, despite being from early and late in this interval, show similar distributions with the largest count rates in the sectors approximately perpendicular to the magnetic field direction and slightly in the sunward direction. The particle distributions were even more strongly peaked in the direction perpendicular to the magnetic field in the vicinity of shock passage, as the fifth pie plot, taken right at shock passage, shows (the magnetic field is not indicated in this plot because of an OMNI magnetic field data gap, but as already discussed, the ACE observations clearly show that the field was near radial, i.e., near vertical in this plot, at this time). Such "pancake" distributions, peaked at ∼90° to the magnetic field direction were often observed by GME at quasi-perpendicular shocks (e.g., Richardson & Cane 2010b) and are consistent with the SDA mechanism (e.g., Sarris & van Allen 1974). However, the shock parameters in Table 1 suggest that this was only an oblique shock, at least at ACE and *Wind*.

In their survey for evidence of pancake distributions in GME observations at ∼350 shocks in 1996-2005, Richardson & Cane (2010b) noted that the shock on 2001 January 31 was one of only three cases (all oblique shocks) where such distributions were evident for many hours during the approach of the shock; most commonly, if pancake distributions were present, they were observed within ∼2 hours of shock passage. Although IMP-8 was near to the bow shock, the persistence of these particle anisotropies while IMP-8 was changing position relative to the bow shock, their clear association with the IP shock, and the relative rarity of similar distributions, suggest that connection to the bow shock was not involved, though this cannot be completely ruled out. Also, though not shown here, GME anisotropy observations for 4-22 MeV/n protons and He, and 1.7-12 MeV/n He and heavier ions generally show similar features.

2.1.3. *Wind solar energetic particle observations*

Figure 3 compiles data from the *Wind* spacecraft during the SEP event. This spacecraft observed the shock at 08:35 UT on day 31 (indicated by the black solid vertical line in Figure 3). Similarly to IMP-8/GME, the spin-axis of *Wind* (perpendicular to the ecliptic plane) and the orientation of the 3DP instrument on board this spacecraft (Lin et al. 1995) allow the measurement of angular intensity distributions even when the magnetic field is close to radial. Figure 3 shows (a) ∼130 keV, (b) ∼555 keV, and (c) ∼4.4 MeV ion intensities measured by the Solid-State Telescope (SST) of *Wind*/3DP transformed into the solar wind frame of reference and binned into six pitch angles relative to the local magnetic field direction. The values of the pitch-angle are color-coded and provided in Figure 3h. *Wind*/3DP/SST does not distinguish among the different ion species and therefore, we assume that the intensities shown in Figures 3a-c are dominated by the more abundant protons. The inset panels in (a), (b), and (c) show the pitch-angle cosine distributions (i.e., μ-distributions) formed from the binned ∼130 keV, ∼555 keV, and ∼4.4 MeV ion intensities, respectively. In each inset panel we show, as a function of μ, the intensity measured at each pitch-angle bin normalized to the maximum intensity among the six bins measured during that time interval. Figures 3e-g show magnetic field data as measured by *Wind*/MFI in the GSE coordinates. Figure 3d shows β_p computed combining magnetic field with solar wind proton data from *Wind*/SWE. Red shading indicates those periods when $\beta_p<0.5$. *Wind* also observed the enhanced magnetic fields associated with the SIR present at the onset of the SEP event (the SI within the SIR is indicated by the vertical pink line in Figure 3), and the smooth magnetic field region prior to the arrival of the shock, indicated by the gray bar in Figure 3. Note that within this region, *Wind* observed an episode of out-of-ecliptic field between day 30.9 and day 31.2, with β_p above 0.5, that was not evident at ACE (Figure 1g).

The ∼4 MeV ion intensities (Figure 3c) gradually increased shortly after the occurrence of the solar flare (indicated by the vertical arrows in Figures 3a-c), with anisotropic flows. After the abrupt increase coincident with the SI, ∼4 MeV ion intensities reached a maximum around day ∼29.5 still with anisotropic flows. Throughout the rising and maximum phases of the event, the largest intensities were observed at small pitch angles (green and dark blue traces in Figure 3), which correspond to particles moving in the anti-sunward direction along the magnetic field (with $\mu\sim+1$). Throughout the decaying phase of the event, ∼4 MeV ion intensities for different pitch-angles acquired similar values indicating a more isotropic character of the particle intensities during this phase of the event (but still mainly with anti-sunward flow).

The ∼555 keV ion intensities (Figure 3b) abruptly increased at the time of the SI with extremely large anti-solar anisotropies that persisted until approximately day ∼30.0 when the anisotropies diminished but remained mostly antisunward until the arrival of the shock. There is however no clear local enhancement at shock passage similar to that observed at IMP-8 (Figure 2b). The ∼130 keV ion intensities (Figure 3a) gradually increased after the SI and kept increasing until about ∼4 hours before the shock passage, when an intensity decrease coincided with the end of

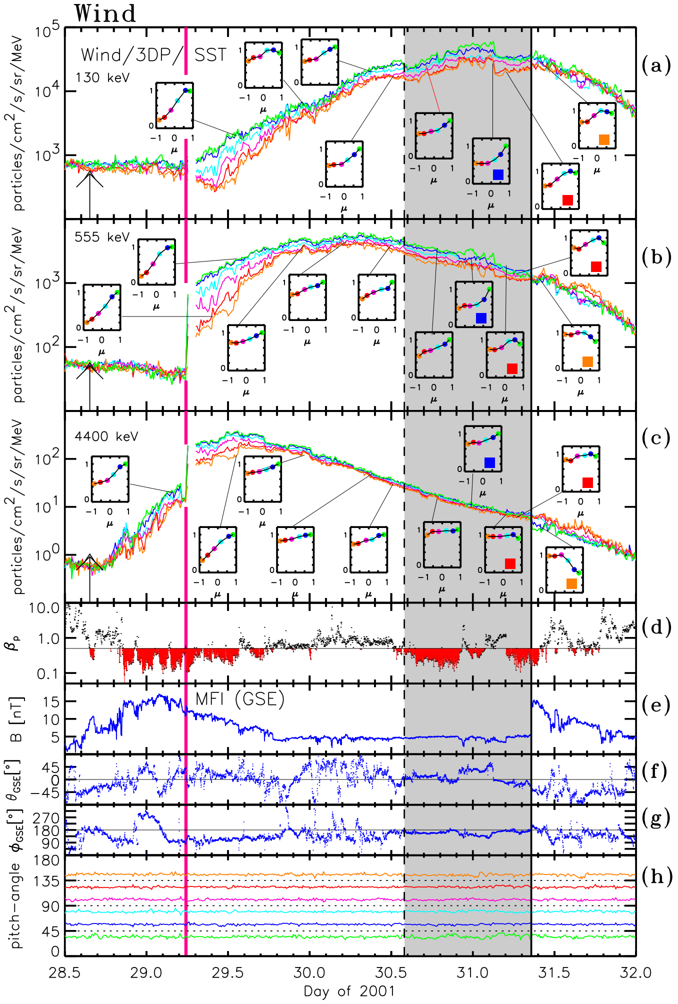

Figure 3. From top to bottom: 10-min averages of the (a) ∼130 keV, (b) ∼555 keV, and (c) ∼4.4 MeV ion intensities in the solar wind frame of reference binned in six different pitch-angles as measured by *Wind*/3DP/SST; (d) proton plasma β_p; 1-min averages of the magnetic field (e) magnitude, (f) polar angle θ_{GSE}, and (g) azimuthal angle ϕ_{GSE} in the GSE coordinate system; (h) pitch angles used to bin the intensities shown in panels (a–c). The insets in panels (a), (b) and (c) show 10-min averages of the μ-distributions generated from the binned ∼130 keV, ∼555 keV, and ∼4.4 MeV ion intensities measured by *Wind*/3DP/SST, respectively. The black solid vertical line indicates the passage of the shock, the dashed vertical line marks the onset of the radial smooth magnetic field region as seen by *Wind*, and the pink vertical solid line the SI of the preceding SIR.

the out-of-the-ecliptic field episode. In contrast to the ∼4 MeV ions that were close to isotropic during the decay of the SEP event, the low-energy ions remained anisotropic with essentially anti-solar flow throughout the event.

The low-energy ion anisotropies at *Wind* show some interesting features in the smooth field region. During the episode of out-of-ecliptic field (between days 30.9 and 31.2), particle anisotropies increased, with PADs more focused around μ∼+1 than just before, as shown in the inset panels identified by blue squares in Figures 3a-c. Then, for a period of ∼6 hours prior to the shock arrival, the μ-distributions (identified by red squares in Figures 3a-c) showed a deficit of ions with small pitch angles (μ∼+1) which can be identified in Figures 3a-c when the dark blue traces remain above the green traces. Such μ-distributions seem consistent with the pancake distributions observed by IMP-8, though in the case of *Wind*, they were observed for a shorter period and were probably interrupted by the out-of-the-ecliptic magnetic field episode, suggesting that at this time *Wind* was observing particles propagating in a different regime than those observed just prior to the shock arrival. It is also possible that during this out-of-the-ecliptic field interval, *Wind* established magnetic connection to portions of the shock front able to accelerate and release particles more easily than the portion of the shock observed in situ by *Wind*, resulting in the increased anti-solar anisotropies.

Because of the lack of magnetic field observations from IMP-8, we do not know whether this out-of-the-ecliptic field region also crossed IMP-8. However, Figure 2a does show a brief interval when the pancake distributions ceased at 03:00–04:45 UT on day 31 (day ∼31.15) that might be evidence for such an encounter.

Immediately behind the shock, the *Wind* ∼4 MeV ion PADs quickly reversed sign, becoming dominated by intensities at μ∼-1 (reddish traces in Figures 3a-c), indicating a sunward flow. At ∼555 keV, the PADs also reversed sign but were more isotropic. This reversal in the PADs agrees with the sunward flow seen downstream of the shock in the IMP-8/GME 0.5-4.0 MeV/n protons and He intensity angular distributions (last pie plot in the top row of Figure 2). By contrast, the ∼130 keV ion PADs continued to be anti-sunward for a period of ∼2 hours after the shock and then became isotropic. We have identified the panels in Figures 3a-c with downstream μ-distributions by orange squares.

2.2. *Suprathermal particle observations*

In this section, we analyze the properties of the ESP event at suprathermal energies ($\lesssim$30 keV) using data from ACE/SWICS, and the High-energy component of the Proton ElectroStatic Analyzer (PESA-H) of the 3DP instrument on board *Wind* (Lin et al. 1995).

2.2.1. *ACE/SWICS suprathermal proton observations*

ACE/SWICS is a linear time-of-flight mass spectrometer with electrostatic deflection that measures the mass, charge, and energy of ions in 60 logarithmical channels scanned every 12 minutes providing a clean particle count rate free of instrumental background. Because of the ACE spin axis, the field of view of SWICS is nearly stationary, pointing nearly radially toward the Sun and sampling a nearly constant section of the sky. This field of view implies that if particles stream along the magnetic field direction, their observation by ACE/SWICS is favored when the magnetic field is close to the radial direction. Details of this instrument can be found in Gloeckler et al. (1998) and Berger (2008).

Figure 4 shows, as a function of time for a period commencing before the start of the smooth field region (dashed vertical line) to 12 hours after shock passage (solid vertical line): (a) proton differential fluxes computed from the count rates measured in the 60 energy channels of ACE/SWICS assuming isotropy and expressed as a function of $1/v$ where v is the proton speed ($1/v$=0.5 s Mm^{-1} corresponds to E∼20 keV; $1/v$=1.0 s Mm^{-1} to E∼5 keV; and $1/v$=1.5 s Mm^{-1} to E∼2.3 keV); (b) differential proton intensities for three artificial ACE/SWICS channels spanning 4.9 to 42.26 keV, generated by summing counts over the indicated energy ranges and assuming isotropic distributions (orange, red and black traces), and spin-averaged differential ion intensities measured in three energy channels of ACE/EPAM/LEMS120 (blue and purple lines); and (c-i) ACE solar wind proton and magnetic field parameters as previously described in relation to Figure 1.

Figure 4a shows that, more than ∼7.35 hours prior to the passage of the shock (starting at day ∼31.0), proton intensities started to increase at the highest energies ACE/SWICS can detect (i.e., E∼80 keV). As indicated by the tilted white dashed line, as the shock approached, the intensity increase was observed at lower and lower energies, reaching $1/v$=1.2 s Mm^{-1} or E∼3.5 keV at the time of shock passage, suggesting that particles arrived at ACE with signatures of velocity dispersion. A straightforward interpretation of this velocity dispersion is that the higher the energy of the protons escaping from the traveling shock front, the earlier they arrived at the spacecraft. Figure 4i shows that, starting at day 30.6, the angle α_R remained below ∼25° until the arrival of the shock, indicating that the magnetic field was oriented close to the radial direction. Assuming the particles were propagating along the magnetic field direction, this field configuration would have favored the observation of particles by ACE/SWICS, even in the case of a narrow field-aligned beam.

2.2.2. *Wind/3DP/PESA-H suprathermal particle observations*

In order to infer pitch-angle distributions in the suprathermal energy regime, we use additional data from *Wind*/3DP/PESA-H. This instrument measures ions at 15 different energies ranging from ∼80 eV to ∼30 keV (the typical energy range of solar wind protons is 500 eV to 28 keV). PESA-H is mounted on a small boom and has an almost unobstructed field of view of the 4π-sky, allowing 3D velocity distribution functions and PADs to be generated (e.g., Wilson et al. 2021). At energies E$\lesssim$1.5 keV, the one-count levels of the detector are too high to observe particles in this low-energy range. Scattered solar UV light might contribute to produce an instrumental background in certain directions. Penetrating higher-energy particles may also contribute to create a background usually observed well before the arrival of shocks in intense SEP events. However, during the passage of shocks associated with intense ESP components, PESA-H registers intensity increases that exceed these background intensities and correspond to

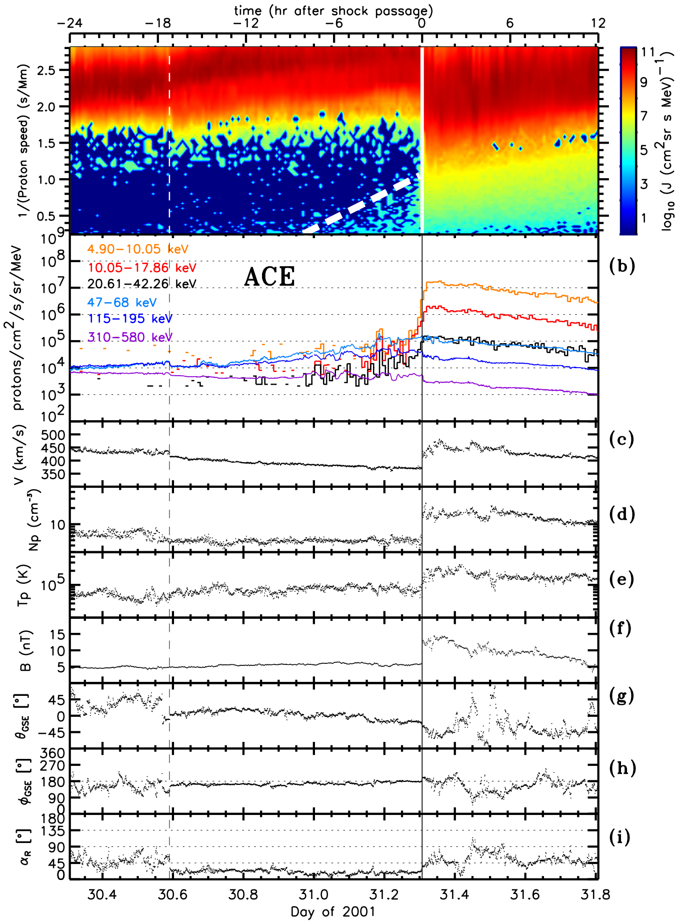

Figure 4. (a) ACE/SWICS proton intensities as a function of $1/v$ where v is the particle velocity; (b) Proton intensities in three artificial ACE/SWICS channels (red, orange and black traces) and 12-min averaged ion intensities measured by ACE/EPAM/LEMS120 (blue and purple traces); (c to i) ACE solar wind proton and magnetic field parameters as in Figure 1. The dashed vertical line indicates the start of the smooth field region. Shock passage is indicated by the solid vertical line. The tilted dashed white line in (a) indicates the velocity dispersion exhibited by the highest energy protons upstream of the shock.

ions in the energy range ∼3–28 keV. Thus, while PESA-H provides a broader field of view than ACE/SWICS, it has an elevated instrumental background that may hinder measurements of weak signals and does not distinguish among ion species, although the measured intensities should be dominated by protons.

Figure 5a shows from top to bottom (a) spin-averaged particle intensities measured by *Wind*/3DP/PESA-H (five top traces) and by *Wind*/3DP/SST (nine bottom traces). The lower panels of Figure 5 show *Wind* magnetic field parameters, as in Figure 3, and solar wind parameters measured by *Wind*/SWE. The solid vertical line indicates the passage of the shock, while the dashed vertical line denotes the onset of the nearly radial, smooth magnetic field region. The vertical dotted lines indicate discontinuities in the solar wind parameters that correspond to abrupt changes in N_p or β_p that were not observed at ACE (Figures 1c and 1e). Not until day ∼30.85 (i.e., ∼12 hr prior to the shock arrival) did PESA-H ion intensities at ∼14 keV increase above the instrumental background intensities observed from the beginning of the time interval plotted in Figure 5. The increase at lower energies ($\lesssim$9 keV) occurred at ∼31.20 (i.e., ∼220 minutes, or ∼3.67 hours, prior to the shock arrival) coincident with a decrease of N_p, an increase of B, and hence a decrease of β_p (last vertical dotted line in Figure 5). Thus, whereas the upstream proton intensity increase measured by ACE/SWICS at similar energies was more gradual (starting about ∼6 hours prior to the shock arrival), the suprathermal intensity increase at *Wind* was more discontinuous, coinciding with changes in B and N_p. Figures 5a and 4b show that the suprathermal ion intensities increased by more than one of order of magnitude peaking at the arrival of the shock. By contrast, at energies $\gtrsim$500 keV, the passage of the shock by *Wind* did not display a significant

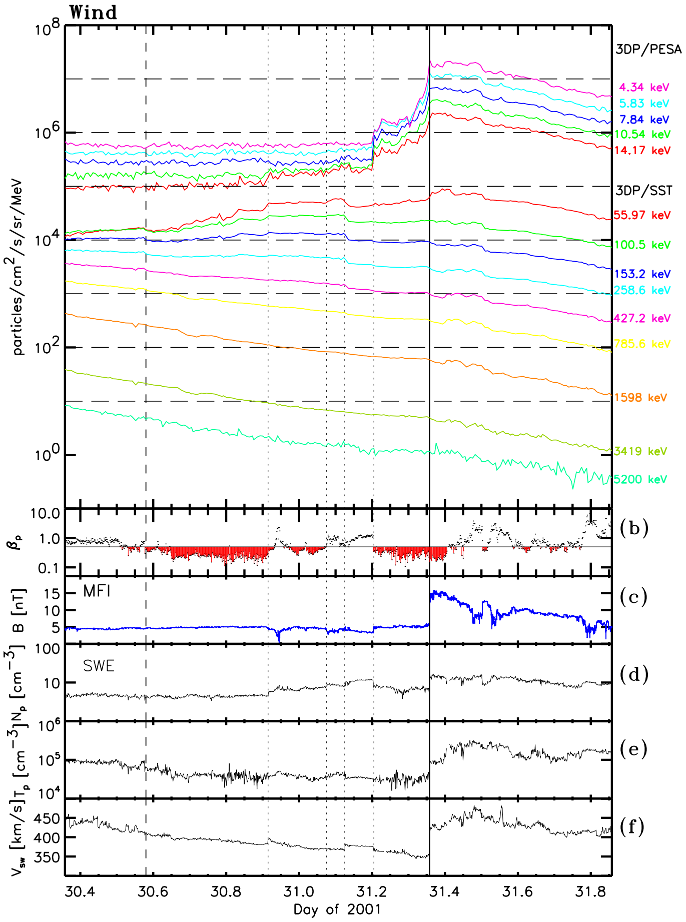

Figure 5. (a) 10-minute averages of the spin-averaged particle intensities at 4.34–14.17 keV measured by *Wind*/3DP/PESA-H (five top traces) and at 55.97–5200 keV measured by *Wind*/3DP/SST (nine bottom traces); (b) β_p, (c) B as measured by *Wind*/MFI, and (d) N_p, (e) T_p, and (f) V_{sw} as measured by *Wind*/SWE. The solid vertical line indicates passage of the shock, and the dashed vertical line denotes the onset of the low-β_p region (as indicated in Figure 3). The vertical dotted lines identify discontinuities in the solar wind parameters that correspond to abrupt changes in N_p and β_p.

enhancement (Figures 5a and 3b), whereas at IMP-8 and ACE there was a small enhancement (Figures 1a, 2b), but not at higher energies (Figure 2d).

Wind/3DP/PESA-H allows us to obtain ion intensities at different pitch-angles. Figure 6 shows, from top to bottom, (a) ~15 keV ion intensities measured by *Wind*/3DP/PESA-H transformed into the solar wind frame of reference and binned into six pitch angles, (b) β_p, (c) B, (d) azimuthal magnetic field angle ϕ_{GSE}, (e) polar magnetic field angle θ_{GSE}, and (f) the pitch-angle values of the similarly colored bins plotted in panel (a). Orange colors correspond to sunward pitch angles (μ~-1) and green/blue correspond to anti-sunward pitch angles (μ~+1). Intervals of large antisunward anisotropies, easily distinguishable in Figure 6a when the ion intensities at different pitch angles are well separated, were observed between day ~30.92 and ~31.13, and especially after day ~31.20 in the increase in intensity extending to the arrival of the shock. Those periods of large anisotropy coincide with changes in the magnetic field. For example, the period with out-of-the-ecliptic magnetic field (i.e. elevated θ_{GSE} in Figure 6e), between the first dotted vertical line at day 30.92 and the third dotted vertical line at day 31.13, particle intensities at energies between ~10 keV and ~200 keV were more elevated, especially for anti-solar pitch angles, than in the prior and subsequent periods (cf. Figure 5). These relatively elevated intensities were observed up to ~200 keV by *Wind*/3DP/SST, but not at energies $\lesssim$10 keV because of the elevated instrumental background of *Wind*/3DP/PESA-H (cf. Figure 5a). Note that prior to day 30.92, β_p acquired low values (β_p<0.5), and after 30.92 β_p oscillated between low and high values. Therefore, the anisotropic character of the ion intensities prior to 31.20 seems to be controlled by discontinuities in the magnetic field rather than by the local value of β_p.

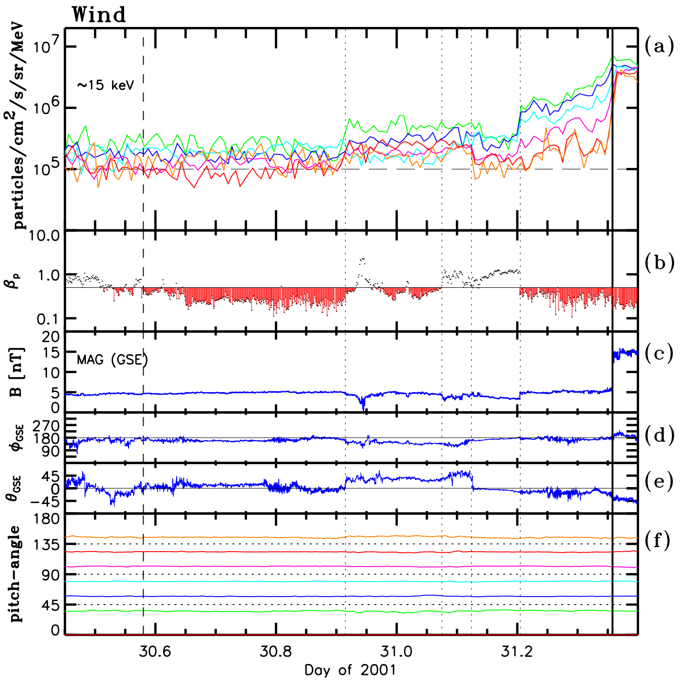

Figure 6. (a) ∼15 keV ion intensities in the solar wind frame of reference binned in six different pitch-angles as measured by *Wind*/3DP/PESA-H; (b) proton plasma β_p; (c) magnetic field magnitude; (d) ϕ_{GSE}; (e) θ_{GSE}; and (f) pitch angles used to bin the intensities shown in panel (a). The solid vertical line indicates the passage of the shock and the dashed vertical line the onset of the radial smooth magnetic field region. The dotted vertical lines indicate discontinuities in the plasma data as identified in Figure 5.

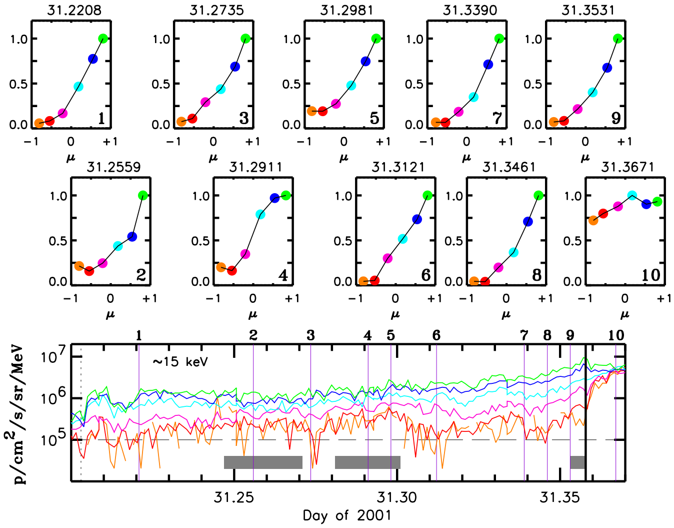

Figure 7. The bottom panel shows ∼15 keV ion intensities in the solar wind frame of reference during the final increase ahead of the shock (the last dotted line in Figure 6 is shown near the beginning of the figure) binned in six different pitch-angles as measured by *Wind*/3DP/PESA-H using the same color scheme as in Figure 6a. The small panels labelled 1-10 show the ∼15 keV ion intensity pitch-angle cosine distributions at the times indicated by the corresponding vertical lines in the bottom panel. The gray rectangles in the bottom panel indicate time intervals with enhanced magnetic field fluctuations (see Section 2.3).

Figure 5a shows that the last intensity increase, observed at day 31.20 (i.e., ∼3.78 hours prior to shock arrival), occurred abruptly at all energies below ∼15 keV, coinciding with an increase of B and a decrease of N_p and hence a decrease of β_p (last dotted vertical line in Figure 5). As already mentioned, this increase was highly anisotropic (Figure 6a) with intensities at different pitch angles separated by almost an order of magnitude, contrasting with the

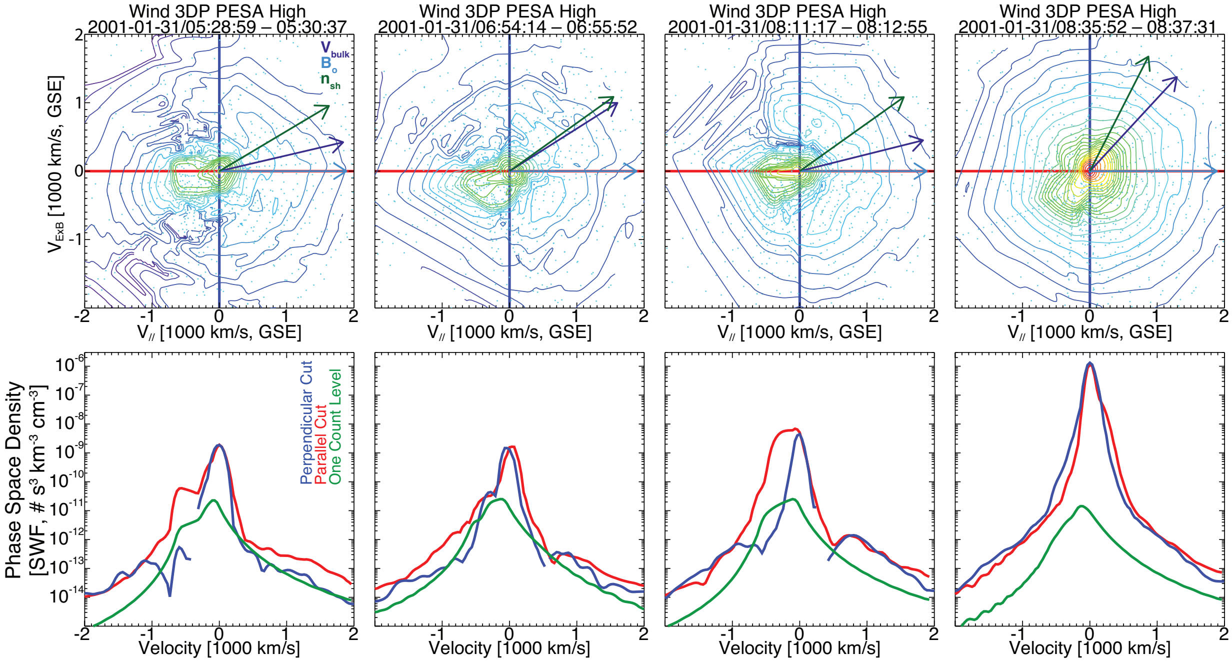

Figure 8. The top panels show contours of constant phase space density (s^3 km^{-3} cm^{-3}) versus velocity in the bulk flow rest frame in the plane formed by $\vec{B}$ and $(\vec{B} \times \vec{V}_{sw}) \times \vec{B}$. The bottom panels show cuts along the parallel (red line) and perpendicular (blue line) magnetic field directions, whereas the green line shows the one-count level (details can be found in Wilson et al. 2013). Projected onto each contour plot are $\vec{V}_{sw}$ (dark blue arrow) and the shock normal $\vec{n}$ (green arrow) obtained from the CfA catalog (Table 1). $\vec{B}$ and $\vec{V}_{sw}$ coordinates used to slice the ion distributions and project $\vec{n}$ and $\vec{V}_{sw}$ are provided in the bottom panels.

moderate anisotropies typically observed prior to quasi-parallel IP shocks for periods of a few tens of minutes (e.g., Sanderson et al. 1985). Figure 7 shows the μ-distributions observed by *Wind*/3DP/PESA-H during this intensity increase. The bottom horizontal panel shows ∼15 keV ion intensities at different pitch angles following the same color scheme as in Figure 6a. The small panels 1 through 10 show the ∼15 keV μ-distributions at the times specified at the top of the panels (also indicated by the purple vertical lines in the bottom panel). We note that throughout the upstream region, ∼15 keV ion intensities displayed large anisotropies with PADs maximizing at $\mu{\sim}{+}1$ (panels 1 through 9), whereas about ∼14 minutes after the shock particle intensities isotropized (panel 10). At some instances during the upstream region, intensities at $\mu{\sim}{-}1$ increased as for example in the μ-distributions shown in panels 2, 4 and 5, that contrast with the other panels where the normalized intensities at $\mu{\sim}{-}1$ were very small (close to 0). We have indicated these periods where the reddish traces ($\mu{\sim}{-}1$) increase by the horizontal gray bars in the bottom panel of Figure 7. Those periods correspond to time intervals with enhanced field fluctuations as discussed below in Section 2.3.

An alternative view of the low-energy ion distributions makes use of the almost unobstructed 4π-sr *Wind*/3DP/PESA-H field of view that allows the generation of 3D phase-space ion velocity distributions (Wilson et al. 2010, 2013). The top panels of Figure 8 show 2D slices of the ion distributions (in the solar wind frame) plotted as contours of constant phase-space density versus velocity (the axes range from ±2000 km s^{-1}) into the plane formed by $\vec{B}$ and $(\vec{B} \times \vec{V}_{sw}) \times \vec{B}$. The horizontal axis indicates the direction parallel to the magnetic field. The dark blue and green arrows indicate the projections of the solar wind velocity $\vec{V}_{sw}$ and shock normal $\vec{n}$ (obtained from the CfA catalog as listed in Table 1), respectively. Each panel contains ∼100 s measurements of data from *Wind*/3DP/PESA-H and uses averages over the indicated time interval of $\vec{B}$ and $\vec{V}_{SW}$ as measured by *Wind*/MFI and *Wind*/SWE, respectively. The bottom panels of Figure 8 show cuts of the velocity distributions parallel (red line) and perpendicular (blue line) to the magnetic field direction. The green line indicates the one-count level. The first three distributions correspond to periods prior to the shock arrival, whereas the last is from immediately following shock passage. The solar wind core is clearly identified in the center of each distribution. An upstream beam, clearly separated from the core population, extending up to speeds above ∼1000 km s^{-1} in the looking-direction antiparallel to $\vec{B}$ (corresponding

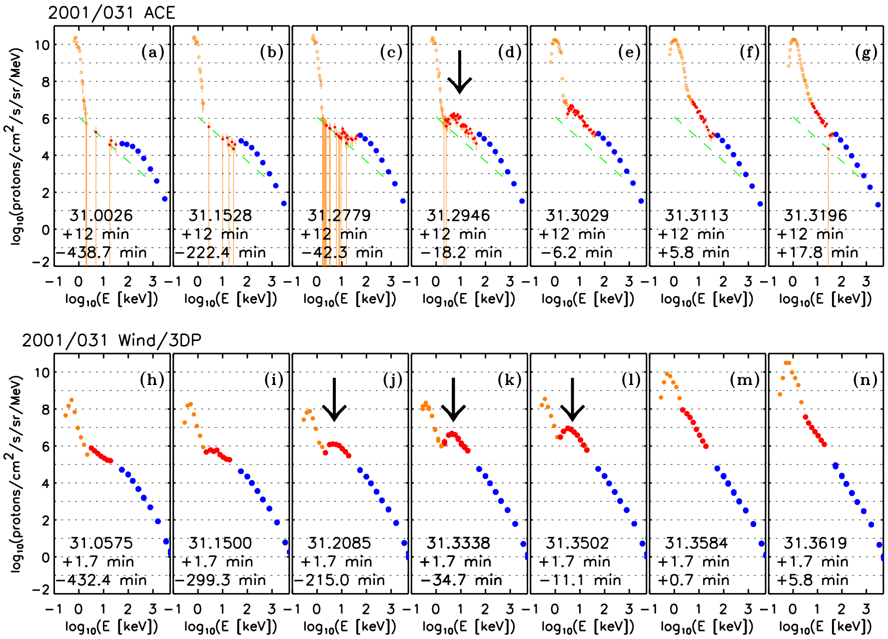

Figure 9. Energy spectra of thermal (orange), suprathermal (red) and energetic particle (blue) populations in the spacecraft frame of reference at different times prior to and after the shock passage. Panels (a-g) show proton measurements from ACE/SWICS (orange and red dots), and spin-averaged ion intensities from ACE/EPAM/LEMS120 (blue symbols). The time in each panel (a-g) indicates the initial time (in units of fractional day of the year) of the 12-minutes over which ACE/SWICS data have been collected and ACE/EPAM averaged. The tilted dashed green lines indicate the one-count level of ACE/SWICS in the suprathermal energy regime. The orange thin lines indicate the error bar associated with each point based on Poisson statistics. Panels (h-n) show spin-averaged ion intensities measured by *Wind*/3DP/PESA-H (orange and red dots) and *Wind*/3DP/SST (blue symbols). The time in each panel (h-n) indicates the initial time (in units of fractional day of the year) of the 1 min 40 sec over which *Wind*/3DP data has been averaged. The +/- time indicated at the bottom of each panel (in units of minutes) is the initial time covered in each panel with respect to the the shock passage at each respective spacecraft (negative values are for times prior to the shock passage and positive values after the shock passage). The black arrows indicate the hump observed in the energy spectra upstream of the shock.

to particles moving in the anti-sunward direction) can be distinguished from the core population (note that a ∼1000 km s^{-1} proton in the solar wind frame would correspond to an energy of ∼10 keV in the spacecraft frame of reference). Whereas the upstream beam appears in the velocity distributions with a clear distinct peak separated from the solar wind core in the left column of Figure 8, closer to the shock (third column in Figure 8) the velocity distribution evolves more continuously from thermal to suprathermal speeds. This low-energy beam was observed starting around day ∼31.2 when low-energy *Wind*/3DP/PESA-H ion intensities increased above the background coincident with changes in B and N_p (Figure 6). Therefore, the beam at these low-energies extended for more than ∼220 minutes (∼3.7 hours) before the shock arrival. The ∼15 keV ion intensities started increasing about ∼10.5 hours prior to the shock, but the structured medium observed upstream of the shock by *Wind* (Figure 6) makes the observation of the beam at these energies discontinuous.

2.2.3. *Energy spectra evolution across the shock*

Another way of examining the evolution of the suprathermal ion population and its relation with the energetic particle populations is to consider the energy spectra. The top row of Figure 9 displays the proton energy spectra observed by ACE/SWICS (orange and red dots) and the spin-averaged ion energy spectra measured by ACE/EPAM/LEMS120 (blue dots) at different times around the passage of the shock. The figures cover an energy range of 0.1 keV to 10 MeV. The orange and red dots distinguish those ACE/SWICS data points in the thermal and suprathermal regimes, respectively. The two components are distinguished by fitting a Gaussian function to the thermal component. The suprathermal component then starts when the spectrum departs from the Gaussian profile. The green dashed straight line indicates the one-count level of ACE/SWICS in the suprathermal regime. Each panel contains a 12-minute interval in which ACE/SWICS scanned all energies sampled by this instrument. The label in each panel indicates the initial time (in units of fractional day) of the 12-minute interval; ACE/EPAM data have been averaged over the same interval. The time before (negative values) or after shock passage (positive values) is also indicated. The thermal component of the spectra (orange dots) may differ from solar wind measurements from ACE/SWEPAM because ACE/SWICS was not designed to measure the solar wind thermal protons. The suprathermal portion of the energy spectrum (red dots) was gradually populated as the shock approached the spacecraft, starting at high energies and displaying a bump (indicated by the black arrow in the spectrum of Figure 9d) that peaked below 10 keV just before the arrival of the shock. Figure 9e covers a 12-minute interval that starts upstream but spans a large fraction of the downstream region, and Figures 9f and 9g continue in the downstream region where the spectra extended smoothly from the suprathermal into the energetic particle range.

The bottom row of Figure 9 displays the spin-averaged ion energy spectra measured by *Wind*/3DP/PESA-H (red and orange dots) and *Wind*/3DP/SST (blue dots) in the spacecraft frame of reference. Similar to ACE/SWICS, PESA-H was not designed to measure the thermal portion of the solar wind spectra, which is indicated with the orange symbols. Each panel covers 100 seconds of data starting at the time indicated in each panel (note that these times do not match those in the upper row). Far from the shock, PESA-H instrumental background intensities affected the suprathermal portion of the spectra (Figures 9h and 9i). Around 220 minutes prior to shock passage (Figure 9j), the energy spectrum acquired a well developed bump around ∼6 keV (indicated by the black arrow in Figures 9j, 9k and 9l) similar to that observed at ACE. Downstream of the shock (Figures 9m and 9n), the suprathermal and energetic particle energy spectra were power-laws $\propto E^{-1.9\pm0.3}$ over the energy range 55-400 keV.

The formation of a bump in the energy spectra upstream of the shock (black arrows in Figure 9) is a consequence of the inability of the low-energy particles to escape from the shock, resulting in a deficit of low-energy particles just above the thermal population). The energy at which this bump is observed depends on the relative difference between the velocity of the escaping particles along the upstream field lines and the speed of the shock parallel to these field lines (see similar examples in Lario et al. 2019). The width of this bump and its separation from the thermal component also depend on the level of magnetic fluctuations upstream of the shock (Trotta et al. 2021).

2.3. *Extended foreshock region*

We now consider in more detail, particle and magnetic field conditions during the extended foreshock region of the 2001 January 31 shock. The proton intensity enhancement in the suprathermal energy regime above the sensitivity of ACE/SWICS was observed for ∼7 hours prior to shock passage for ∼80 keV protons but for only ∼220 minutes (3.67 hours) for $\lesssim$10 keV protons (cf. Figure 4). Therefore, the extent of the foreshock region at ACE was energy dependent. At *Wind*, the foreshock region was more disturbed than at ACE, with discontinuous enhancements of ion intensities responding to plasma and field fluctuations (Figures 5 and 6). The final ion intensity enhancement prior to the shock arrival at *Wind* occurred at day 31.20 (indicated by the last dotted vertical line in Figures 5 and 6). Figure 10 shows in detail the interval from this final intensity increase until just after shock passage. In particular, we show (a) ∼5 keV and (b) ∼15 keV ion intensities in the solar wind frame of reference, binned in six different pitch-angles, as measured by *Wind*/3DP/PESA-H (using the same color code as in Figures 6 and 7), (c) $\delta B/\langle B\rangle$, where $\delta B = \left[\sum_{i=1}^{3} (\delta B_i)^2\right]^{1/2}$, and $\delta B_i = B_i - \langle B_i\rangle$, where B_i is one of the components of the vector $\vec{B}$ in the GSE coordinate system, and $\langle\rangle$ indicates the average computed over the time interval between day 31.205 and the shock arrival, (d) $\delta B_x/\langle B\rangle$, (e) $\delta B_y/\langle B\rangle$, (f) $\delta B_z/\langle B\rangle$, (g) ϕ_{GSE}, and (h) θ_{GSE}. Magnetic field variations δB and δB_i have been computed using *Wind*/MFI field data with a time resolution of 0.092 seconds. Figure 10 shows that most of the magnetic field oscillations during the last ion intensity enhancement prior to the shock arrival occurred in the y and z directions, i.e., mostly perpendicular to the mean field that was close to the radial direction. They were most prominent in two intervals of enhanced fluctuations (indicated by gray rectangles in Figure 10c and also in Figure 7) between day ∼31.25 and ∼31.27 and between day ∼31.28 and ∼31.30 (also seen in the fluctuating values of θ_{GSE}), and in a short region of enhanced fluctuations just before the arrival of the shock, also indicated by a gray rectangle. During these periods, the ∼15 keV ions became less anisotropic, as indicated by the increase in intensities for the pitch angles represented by the reddish traces relative to the intensities for other pitch angles in Figure 10b. The ∼5 keV ion intensities (Figure 10a) displayed also large anisotropies, especially in the last intensity increase prior to the shock at day ∼31.32 (i.e., about ∼60 minutes before the shock arrival). Note that the ∼5 keV reddish traces (μ∼-1) increased also during the time intervals indicated by the gray rectangles.

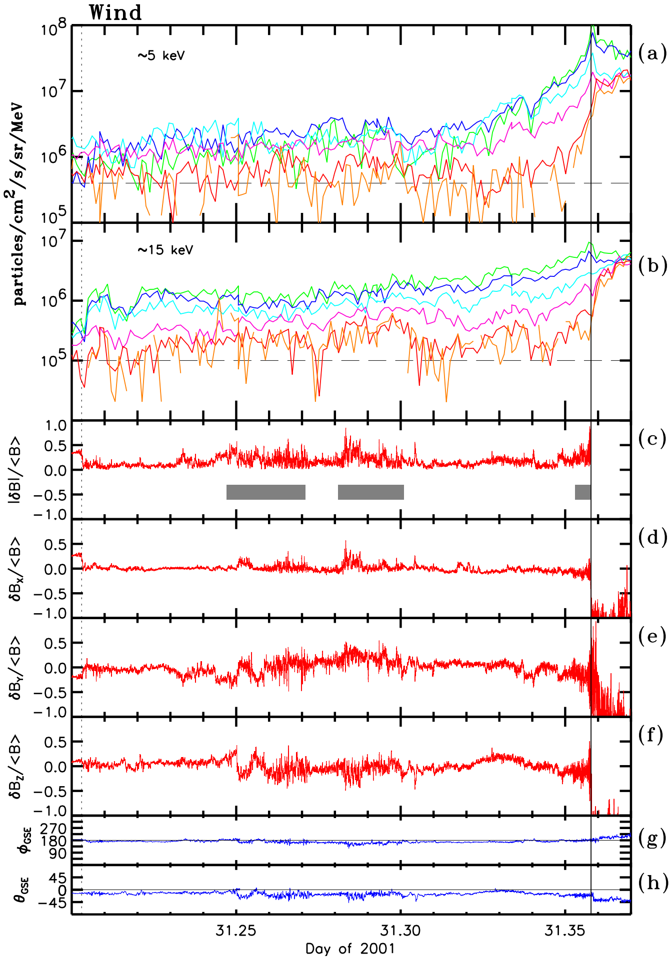

Figure 10. (a) ∼4.5 keV ion intensities in the solar wind frame of reference binned in six different pitch-angles as measured by *Wind*/3DP/PESA-H using the same color code as in Figures 2 and 4; (b) ∼14.8 keV ion intensities in the solar wind frame of reference binned in six different pitch-angles as measured by *Wind*/3DP/PESA-H using the same color code as in Figures 2 and 4; (c) δB/<B>, (d) δB_x/<B>, (e) δB_y/<B>, (f) δB_z/<B>, (g) magnetic field azimuthal angle ϕ_{GSE}; (h) magnetic field polar angle θ_{GSE}. Over the time interval between 31.205 (dotted vertical line) and the shock arrival, the averaged magnetic field in GSE coordinates is $<\vec{B}>=(-4.73\pm0.56,0.85\pm0.84,-1.30\pm0.78)$ nT. The gray rectangles in panel (c) indicate time intervals with enhanced magnetic field fluctuations.

As already noted, magnetic field fluctuations in the first two time intervals indicated in Figure 10c were primarily in the y and z GSE components, implying a wave vector mostly along the x-GSE direction propagating in the anti-sunward direction, i.e., along the background quasi-static magnetic field. Analyses of the magnetic field power spectra (not shown here) show that the transverse power was about two orders of magnitude stronger than the compressional power, peaking at about 0.01-0.03 Hz in the spacecraft frame of reference. Whereas the observed waves were mostly left-handed polarized with negative ellipticities, they also displayed positive ellipticities in some frequencies and/or time intervals. Some aspects of these fluctuations could be related to fluctuations observed upstream of IP shocks generated by field-aligned beams (e.g., Jian et al. 2009; Kajdič et al. 2012; Blanco-Cano et al. 2016, and references therein), although in our case they cannot be classified as coherent ion-scale cyclotron waves because of their intermittency and far from circular ellipticities.

Immediately before the shock arrival, there was also an increase of field fluctuations, but at a higher frequency than those observed farther upstream of the shock and involving also field magnitude B fluctuations. Figure 11 shows the evolution of the field magnitude and components around the shock arrival. In particular, we show, from top to bottom, (a) B, the three components of $\vec{B}$ in GSE coordinates (b) B_{xGSE}, (c) B_{yGSE}, (d) B_{zGSE}, and the three components of $\vec{B}$ in the shock normal coordinates, (e) B_n, (f) B_l, (g) B_m. B_n points along the shock normal, B_l is parallel to the projection of the averaged upstream interplanetary magnetic field onto the plane of the shock, and B_m completes the

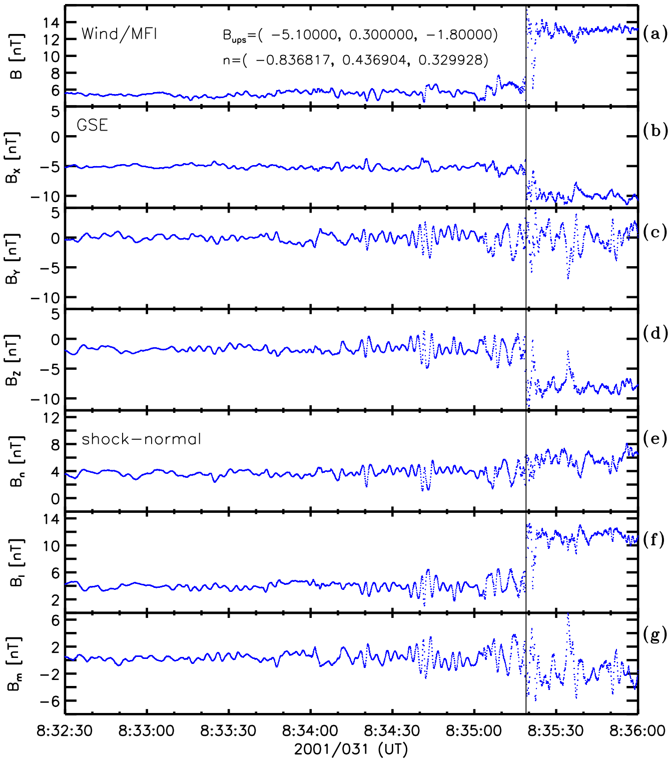

Figure 11. 0.092 second measurements of (a) B, (b) B$_{xGSE}$, (c) B$_{yGSE}$, (d) B$_{zGSE}$, (e) B$_n$, (c) B$_l$, (d) B$_m$, as measured by *Wind*/MFI around the arrival of the shock indicated by the solid vertical line.

right-hand system. Upstream magnetic field coordinates used to perform such rotation are indicated in Figure 11a as listed in the CfA catalog when solving the RH equations to find the shock parameters. Whereas low frequency waves appeared as early as ∼20 min before the shock arrival, the amplitude of the field fluctuations increased in the last 2 minutes before the shock passage. In the spacecraft frame of reference, the estimated frequency was about 0.2-0.7 Hz ∼35 seconds before the shock arrival and 2-3 Hz immediately at the shock arrival. The higher frequency, the frequency dispersion with higher frequencies closer to the shock ramp, and the changes in B concurrent with the component fluctuations, indicate that the field fluctuations immediately adjacent to the shock were whistler precursors typically observed very close to IP shocks (e.g., Wilson et al. 2017). Therefore, field fluctuations immediately upstream of the shock were of a different nature from those observed far upstream.

3. DISCUSSION

The general properties of ESP events depend upon the processes of particle acceleration at the approaching shock, the presence of a seed population of particles being injected into these particle acceleration processes, the mechanisms that allow the particles to escape from the vicinity of the shock, the presence of intervening IP structures affecting the transport of shock-accelerated particles toward the spacecraft, and the level of turbulence of the medium through which the shock and the shock-accelerated particles propagate. Trotta et al. (2021) investigated the processes of interaction between shock and upstream magnetic field fluctuations and determined the role played by magnetic field turbulence in the upstream particle transport. In particular, they showed that the particle transport strongly depends on the upstream turbulence properties, where different turbulence patterns may act as transport corridors or barriers, and hence modify the characteristics of ESP events. In addition, upstream fluctuations convected into the shock front are able to induce strong changes in the local shock geometry, further complicating the picture of creation and propagation of field-aligned beams (e.g., Kajdič et al. 2019).

We suggest that the steady, smooth radially-orientated magnetic field upstream of the shock on 2001 January 31 (Figures 1f-i), provided the appropriate conditions for the observation of a field-aligned ion beam over a wide range of energies in an extended region upstream of the shock. This quiet, radial magnetic field region was most likely formed at the tail of a modest high-speed (∼500 km s^{-1}) solar wind stream observed by ACE, IMP-8 and *Wind* on January

29-30 (similar examples of quiet field intervals at the tail of fast solar wind streams can be found in, e.g., Borovsky & Denton 2016; Carnevale et al. 2021, and references therein). Also, although not directly related to the ESP event, we note that a SIR lying at the leading edge of this stream passed the spacecraft on January 28-29, and influenced the arrival of SEPs at the three spacecraft following the solar eruption on 2001 January 28 that was responsible for the IP shock observed in situ on day 31. In particular, the passage of the stream interface within this SIR was associated with an abrupt increase in the intensity of $\lesssim$4 MeV ions at 1 au, suggesting that these ions could propagate to 1 au more efficiently within the high-speed stream than in the preceding slower solar wind. In contrast, $\gtrsim$25 MeV ions populated both slow and high-speed streams. Discontinuities of particle intensities coinciding with the SI of SIRs have been previously observed at different heliocentric distances and latitudes (e.g., Intriligator et al. 1995, 2001). The fact that the time-intensity profiles of the near-relativistic electrons during this SEP event (not shown here) resemble those of the high ($\gtrsim$25 MeV) energy protons (Figure 2d) suggests that the particle speed rather than particle gyroradius played a more relevant role in the arrival of particles at each spacecraft across the passage of the SI.

The continuous injection of particles by traveling IP shocks favors the observation of long-lasting particle anisotropies in SEP events, especially for the low energy particles that shocks are thought to accelerate more efficiently (Heras et al. 1994). The conditions in the background plasma through which the particles propagate and the ability of streaming particles to enhance magnetic field fluctuations are factors that may determine the transport conditions for particles leaving the shock vicinity, and hence whether large anisotropies are observed by a distant spacecraft (e.g. Lee 1971; Ng et al. 2012). In particular, Reames et al. (2001) suggested that particle streaming is organized by the value of β_p, with a value 0.5 discriminating between a turbulent plasma (where $\beta_p>0.5$) and plasma with low magnetic field fluctuations ($\beta_p<0.5$). Low-β_p, characterized by a lack of magnetic turbulence, is then expected to favor free particle streaming, and hence the observation of anisotropic flows. Figure 3 shows that, at the onset of the SEP event, $\beta_p<0.5$ coincided with the observation of anisotropic flows. β_p increased above 0.5 around day 29.75 (at the trailing edge of the SIR) and the ion distributions became more isotropic but still with anti-sunward flows. However, the ~130 keV and ~555 keV ion intensities became anisotropic again at around day ~30.25 when β_p was still >0.5 (Figures 3a-b). The decaying ~4.4 MeV ion intensities were more isotropic regardless of the β_p value. Therefore, we attribute the fact that large anisotropies were more persistent at low (Figures 3a-b) than at high energies (Figure 3c) during this SEP event to the continuous injection of low-energy particles from the approaching shock rather than the local measurement of β_p.

The entry into the quiet radial magnetic field upstream of the shock (gray bar in Figures 1- 3) did entail a change in the pitch-angle distributions observed during the SEP event, especially at high ($\gtrsim$500 keV) energies. For a period of ~16 hours prior to the shock during this smooth magnetic field region, and extending to shock passage but not beyond, IMP-8/GME observed unusual energetic ion angular distributions, where the largest count rates were observed in sectors approximately perpendicular to the magnetic field direction. These IMP-8/GME pancake angular distributions were observed for 0.5-4.0 MeV/n protons+He intensities (Figures 2a), but also for 4-22 MeV/n protons and He, and 1.7-12 MeV/n He and heavier ions. Pitch-angle distributions from *Wind*/3DP/SST also indicated a reduction in intensity at small pitch angles parallel or anti-parallel to the magnetic field ($|\mu|\sim1$), but only for a period of ~6 hours prior to the shock (as shown by the μ-distributions indicated by red squares in the inset panels in Figures 3a-c). Such a deficit of particles with $|\mu|\sim1$ at *Wind* was more pronounced for ~555 keV ions than for ~130 keV ions, and occurred after a period of out-of-ecliptic magnetic field orientations. Most likely particles arriving at *Wind* during this out-of-the-ecliptic field excursion experienced different transport conditions than those observed during the ~6 hours prior to shock arrival.

A possible explanation for these pancake-like ion distributions is that the quiet magnetic fields in the radial field region resulted in a near scatter-free transport of particles, allowing small pitch-angle ions to escape from this region while large pitch-angle ions remained. This is somewhat analogous to the formation of pancake ion distributions in the lobes of the geomagnetic tail, also characterized by low variance magnetic fields (Owen et al. 1990, 1991). As particles escape from the approaching shock, the decreasing magnetic field magnitude with radial distance leads the particles to be focused along the magnetic field direction, until they reach the trailing edge of the preceding SIR, now located beyond 1 au, where the increased magnetic field magnitude causes the particles to be reflected. Assuming that the magnetic field magnitude in the SIR is similar to the magnetic field observed downstream of the shock at its passage by 1 au (~15 nT) and that the magnetic field between these two enhanced field regions reaches a minimum around ~5 nT (cf. Figure 3e), one can estimate that particles with pitch angles $\gtrsim35°$ remained confined within this magnetic bottle. The larger the speed of the particles, the more likely they (at least those with smaller pitch angles) were to reach the SIR, resulting in pancake-like angular distributions that were more evident at higher ($\gtrsim$500 keV) than at lower ($\lesssim$100 keV) energies. The continuous and more efficient injection of low-energy particles in the anti-sunward direction by the approaching shock implies that the difference between the intensities with $\mu\sim+1$ and $\mu\sim$-1 was more prominent at lower energies (Figure 3a) than at higher energies (Figure 3c), and hence, the event was more anisotropic at low energies.

The anisotropic character of the SEP event at ∼130 keV energies was also observed in the suprathermal energy ($\lesssim$30 keV) regime but only for a short time interval before the shock passage. The orientation of the magnetic field prior to the arrival of the shock favored the observation of upstream suprathermal particles by ACE/SWICS (Figure 4). The upstream time interval when these suprathermal protons were observed by ACE/SWICS (above a clean pre-event background intensities dominated by zero-count intensities in the suprathermal regime; see Figures 4a, 4b, and 9a) varied from about ∼7 hours before the shock arrival for ∼80 keV protons to ∼240 minutes before the shock arrival for ∼10 keV protons (at ∼20 keV, ACE/SWICS intensities were observed to increase ∼300 minutes before the shock). Therefore, the arrival of foreshock particles at ACE exhibited velocity dispersion similar to that at the onset of SEP events (cf. Figure 4a). This velocity dispersion effect might result if higher-energy particles in the upstream proton distribution extended further upstream of the shock than lower-energy particles. The intensity of these particles decayed with distance from the shock, remaining below the sensitivity of ACE/SWICS or below the *Wind*/3DP/PESA-H background for longer distances.

However, the upstream proton intensity increase was not observed at energies $\lesssim$3 keV. In fact, the particle energy spectra observed before the shock arrival exhibited a bump at energies ∼6–10 keV (Figures 9d, 9k and 9l) characteristic of the energy spectra observed in the suprathermal regime upstream of oblique shocks (Giacalone et al. 1993; Lario et al. 2019). These energy spectra might develop as a consequence of the ability of particles to escape from the vicinity of oblique shocks (e.g., Burgess 1995). Low-energy particles propagating along magnetic field lines are unable to propagate long distances upstream of the shock because the shock motion overtakes them, whereas higher-energy particles are able to run away from the shock. The relative difference between the speed of the particles parallel to the magnetic field and the shock speed along the upstream field lines marks the energy at which the bump of the energy spectra develops (e.g., Lario et al. 2019). The low turbulence levels found upstream of the shock on 2001 January 31 also favor the development of this bump in the energy spectra. The propagation of particles in an unperturbed upstream medium results in energy spectra where particles escaping from the shock are well separated from the thermal population, whereas in more turbulent media, shock-accelerated particles spread their energy in phase space, resulting in a more extended energy spectra where thermal and shock-accelerated populations blend (Trotta et al. 2021). Velocity distribution functions shown in the bottom panels of Figure 8 allow the thermal particles and those that constitute the field-aligned beam to be distinguished (an ∼3(6) keV proton in the spacecraft frame of reference would correspond to a ∼400(700) km s^{-1} proton in the solar wind frame of reference used in Figure 8). However, this distinct peak is not always continuously observed as in some distributions it appears as an extension of the thermal population (third column in Figure 8), which may depend on the local properties of the medium.

The sporadic changes in the field orientations observed by *Wind* in the foreshock region led to abrupt increases of particle intensities, especially at low energies $\lesssim$15 keV. This is particularly evident at the final particle enhancement just before the shock, where the particle increase coincided with a decrease of N_p, increase of B, and hence a decrease of β_p (Figure 5). The anisotropic character of the event at *Wind* was affected by these plasma and magnetic field discontinuities rather than local changes in β_p (Figure 6). The final suprathermal particle increase at *Wind* just before shock arrival (after day 31.20, cf. Figure 5) was highly anisotropic, with particle intensities varying by one order of magnitude for different pitch angles (Figure 7). The final intensity enhancement just prior to the shock arrival was much more anisotropic for ∼15 keV ions, with PADs more focused toward $\mu\sim+1$ as shown in Figure 7, than for ∼130 keV ions (Figure 3a). Since intensity enhancements were observed also for pitch angles close to 90° ($\mu\sim0$) (Figure 7), the use of "beam" to describe these ion distributions should be understood in its broader sense, implying a certain width for a relatively collimated flow of particles along the magnetic field direction. The arrival of particles with $\mu\sim0$ at the spacecraft might result from their finite gyroradii as well as possible small scatters as they propagate from the shock to the spacecraft.

Whereas the foreshock smooth magnetic field region might have favored the nearly scatter-free transport of particles injected from the shock, isolated periods of enhanced magnetic field fluctuations observed by *Wind* (first two gray bars in Figure 10c) still affected these particles, reducing their anisotropy. It is possible that these field fluctuations far upstream were enhanced by the propagating particles. Alternatively, they may have been intrinsic to the solar wind in these intervals and thus affected the transport of the suprathermal particles. As the shock approached the spacecraft, the ion distributions intensified mostly at pitch angles with $\mu>0$ (Figures 10a and 10b), but also for $\mu\sim$-1 just $\sim$6 minutes before the shock (last gray rectangle in Figure 10c). The close proximity of the shock continuously injecting low-energy particles was most likely responsible for this final intensity increase. Whistler pre-shock fluctuations were observed just for less than a couple of minutes prior to the shock arrival (Figure 11). Whistler precursors can be driven by both dispersive radiation from the shock and modified two-stream instabilities. The latter are usually due to shock-reflected ions near the shock ramp but these cannot excite waves further upstream because of the decreasing beam density with distance from the shock.

Apart from the particle transport conditions in the upstream smooth magnetic field region, the evolution of both the suprathermal ($\lesssim$30 keV) and the energetic ($\gtrsim$50 keV) particle populations (Figure 5) is determined also by the efficiency of the shock as particle accelerator. The large upstream anisotropies observed at low energies ($\lesssim$130 keV) by *Wind*, although affected by changes in the magnetic field (such as the out-of-ecliptic field excursion), indicate that these particles were continuously injected by the approaching shock. The pronounced peak in the $\lesssim$15 keV ion intensities at the shock passage (Figure 10) suggests that, as its arrival at 1 au, the shock was an efficient accelerator in the suprathermal energy regime (whereas at energies $\gtrsim$130 keV, the shock was not so efficient as shown in Figure 5 and in the unchanging particle spectra at energies $\gtrsim$100 keV displayed by blue symbols in Figure 9). On the other hand, the IMP-8/GME observations do show a small enhancement of >0.5 MeV/n ions in the vicinity of shock passage (Figure 2b), suggesting that there was energetic particle acceleration at the location of this spacecraft. Apart from the shock parameters, the efficiency of the shock in particle acceleration may depend also on the presence of a seed population of particles being injected into the acceleration processes. The fact that ACE/SWICS only observed suprathermal particles above its one-count level sensitivity a few hours before the shock (Figure 4) and that *Wind*/3DP/PESA-H observed only an increase above the elevated instrumental background coinciding with B and N_p discontinuities (Figure 5) prevents us from identifying suprathermal seed populations far from the shock arrival. The large SEP event with onset on day 28 may have supplied abundant particles for the IP shock to reaccelerate in its way to 1 au. The lack of magnetic field oscillations in the extended foreshock region indicates that the beam of particles accelerated by the shock was not intense enough to drive strong instabilities that would have grown to a sufficient amplitude before convected back to the shock and thus favoring the scatter of particles leading to multiple interactions with the shock. Therefore, whereas it is possible that the SEP event may have provided an abundant seed population (not observed by ACE/SWICS or *Wind*/3DP/PESA-H far from the shock), the efficiency of the shock in particle acceleration may have been limited by the easy escape of particles from the shock vicinity.

4. SUMMARY

The ESP event observed by ACE, *Wind* and IMP-8 in association with the passage of the interplanetary shock on 2001 January 31 showed several unusual features: (i) A region extending $\sim$16 hours upstream of the shock characterized by a smooth radial magnetic field in the tail of a modest high-speed solar wind stream, (ii) an anisotropic low-energy particle intensity increase observed upstream of the shock for an extended time interval, and (iii) a higher-energy particle population trapped within this quiet field region. We suggest that the continuous injection of particles by the traveling shock into the quiet field region produced this extended foreshock region, with a spatial extent that depended on the energy of the particles. In the absence of enhanced magnetic field fluctuations upstream of the shock, particle scattering was likely to be infrequent, allowing the particles with small pitch-angles ($\mu\sim1$) to escape from the shock and thus lead to the observation of an extended anisotropic, field-aligned beam at low ($\lesssim$30 keV) energies. Only during short time intervals at *Wind* when field fluctuations were enhanced, did the $\lesssim$30 keV ion anisotropies diminish somewhat. The presence of a more perturbed region lying ahead of the quiet field region allows the escape of the more mobile high-energy particles with large pitch-angle cosine ($|\mu|\sim1$) but confine particles with small pitch-angle cosine ($\mu\sim0$) and hence the observation of pancake ion distributions at high ($\gtrsim$500 keV) energies.

ACKNOWLEDGMENTS

D.L. and I.G.R. acknowledge support from NASA Living With a Star (LWS) programs NNH17ZDA001N-LWS and NNH19ZDA001N-LWS, the Goddard Space Flight Center Internal Scientist Funding Model (competitive work package) program and the Heliophysics Innovation Fund (HIF) program. I.G.R also acknowledges support from the ACE mission. L.K.J. thanks the support of NASA LWS and Heliophysics Supporting Research (HSR) programs. The data used in this paper can be downloaded from spdf.gsfc.nasa.gov, and www.srl.caltech.edu/ACE/ASC/. We acknowledge all of the science instrument teams for making their data used in this paper available.

REFERENCES

Bellomo, A., & Mavretic, A. 1978, MIT Plasma Experiment on IMP H and J Earth Orbited Satellites (MIT Center for Space Research Technical Report CSR-TR-78-2)

Berger, L. 2008, PhD thesis, Christian-Albrechts-Universität zu Kiel

Blanco-Cano, X., Kajdič, P., Aguilar-Rodríguez, E., et al. 2016, Journal of Geophysical Research (Space Physics), 121, 992, doi: 10.1002/2015JA021645

Borovsky, J. E., & Denton, M. H. 2016, Journal of Geophysical Research (Space Physics), 121, 6107, doi: 10.1002/2016JA022863

Brueckner, G. E., Howard, R. A., Koomen, M. J., et al. 1995, SoPh, 162, 357, doi: 10.1007/BF00733434

Bryant, D. A., Cline, T. L., Desai, U. D., & McDonald, F. B. 1962, JGR, 67, 4983, doi: 10.1029/JZ067i013p04983

Burgess, D. 1995, in Introduction to Space Physics, ed. M. G. Kivelson & C. T. Russell (Cambridge: Cambridge University Press), 129–163

Burlaga, L. F. 1974, JGR, 79, 3717, doi: 10.1029/JA079i025p03717

Carnevale, G., Bruno, R., Marino, R., Pietropaolo, E., & Raines, J. M. 2021, arXiv e-prints, arXiv:2108.09552. https://arxiv.org/abs/2108.09552

Cohen, I. J., Schwartz, S. J., Goodrich, K. A., et al. 2019, Journal of Geophysical Research (Space Physics), 124, 3961, doi: 10.1029/2018JA026197

Decker, R. B. 1983, JGR, 88, 9959, doi: 10.1029/JA088iA12p09959

Forsyth, R. J., & Marsch, E. 1999, SSRv, 89, 7, doi: 10.1023/A:1005235626013

Giacalone, J., Burgess, D., Schwartz, S. J., & Ellison, D. C. 1993, ApJ, 402, 550, doi: 10.1086/172157

Gloeckler, G., Cain, J., Ipavich, F. M., et al. 1998, SSRv, 86, 497, doi: 10.1023/A:1005036131689

Gold, R. E., Krimigis, S. M., Hawkins, S. E., I., et al. 1998, SSRv, 86, 541, doi: 10.1023/A:1005088115759

Gosling, J. T. 1983, SSRv, 34, 113, doi: 10.1007/BF00194621

Gosling, J. T., Asbridge, J. R., Bame, S., Paschmann, G., & Sckopke, N. 1978a, GeoRL, 5, 957, doi: 10.1029/GL005i011p00957

Gosling, J. T., Asbridge, J. R., Bame, S. J., & Feldman, W. C. 1978b, JGR, 83, 1401, doi: 10.1029/JA083iA04p01401

Gosling, J. T., Bame, S. J., Feldman, W. C., et al. 1984, JGR, 89, 5409, doi: 10.1029/JA089iA07p05409

Guo, F., Giacalone, J., & Zhao, L. 2021, Frontiers in Astronomy and Space Sciences, 8, 27, doi: 10.3389/fspas.2021.644354

Heras, A. M., Sanahuja, B., Sanderson, T. R., Marsden, R. G., & Wenzel, K. P. 1994, JGR, 99, 43, doi: 10.1029/93JA02826

Intriligator, D. S., Jokipii, J. R., Horbury, T. S., et al. 2001, JGR, 106, 10625, doi: 10.1029/2000JA000070

Intriligator, D. S., Siscoe, G. L., Wibberenz, G., Kunow, H., & Gosling, J. T. 1995, GeoRL, 22, 1173, doi: 10.1029/95GL00951

Ipavich, F. M. 1974, GeoRL, 1, 149, doi: 10.1029/GL001i004p00149

Jian, L. K., Russell, C. T., Luhmann, J. G., et al. 2009, ApJL, 701, L105, doi: 10.1088/0004-637X/701/2/L105

Kajdič, P., Blanco-Cano, X., Aguilar-Rodriguez, E., et al. 2012, Journal of Geophysical Research (Space Physics), 117, A06103, doi: 10.1029/2011JA017381

Kajdič, P., Hietala, H., & Blanco-Cano, X. 2017, ApJL, 849, L27, doi: 10.3847/2041-8213/aa94c6

Kajdič, P., Preisser, L., Blanco-Cano, X., Burgess, D., & Trotta, D. 2019, ApJL, 874, L13, doi: 10.3847/2041-8213/ab0e84

Kallenrode, M. B. 1995, Advances in Space Research, 15, 375, doi: 10.1016/0273-1177(94)00120-P

Kilpua, E. K. J., Lumme, E., Andreeova, K., Isavnin, A., & Koskinen, H. E. J. 2015, Journal of Geophysical Research (Space Physics), 120, 4112, doi: 10.1002/2015JA021138

Koval, A., & Szabo, A. 2008, Journal of Geophysical Research (Space Physics), 113, A10110, doi: 10.1029/2008JA013337

Lario, D., Berger, L., Decker, R. B., et al. 2019, AJ, 158, 12, doi: 10.3847/1538-3881/ab1e49

Lario, D., Berger, L., Wilson, L. B., I., et al. 2018, in Journal of Physics Conference Series, Vol. 1100, Journal of Physics Conference Series, 012014, doi: 10.1088/1742-6596/1100/1/012014

Lario, D., & Decker, R. B. 2002, GeoRL, 29, 1393, doi: 10.1029/2001GL014017

Lario, D., Ho, G. C., Decker, R. B., et al. 2003, in American Institute of Physics Conference Series, Vol. 679, Solar Wind Ten, ed. M. Velli, R. Bruno, F. Malara, & B. Bucci, 640–643, doi: 10.1063/1.1618676

Lario, D., Hu, Q., Ho, G. C., et al. 2005, in ESA Special Publication, Vol. 592, Solar Wind 11/SOHO 16, Connecting Sun and Heliosphere, ed. B. Fleck, T. H. Zurbuchen, & H. Lacoste, 81

Lario, D., & Roelof, E. C. 2010, in American Institute of Physics Conference Series, Vol. 1216, Twelfth International Solar Wind Conference, ed. M. Maksimovic, K. Issautier, N. Meyer-Vernet, M. Moncuquet, & F. Pantellini, 639–642, doi: 10.1063/1.3395947

Lee, M. A. 1971, Plasma Physics, 13, 1079, doi: 10.1088/0032-1028/13/12/001

—. 1983, JGR, 88, 6109, doi: 10.1029/JA088iA08p06109

—. 2005, ApJS, 158, 38, doi: 10.1086/428753

Lepping, R. P., Acũna, M. H., Burlaga, L. F., et al. 1995, SSRv, 71, 207, doi: 10.1007/BF00751330

Lin, R. P., Anderson, K. A., Ashford, S., et al. 1995, SSRv, 71, 125, doi: 10.1007/BF00751328

Marhavilas, P. K., Malandraki, O. E., & Anagnostopoulos, G. C. 2015, Planet. Space Sci., 117, 192, doi: 10.1016/j.pss.2015.06.010

McComas, D. J., Bame, S. J., Barker, P., et al. 1998, SSRv, 86, 563, doi: 10.1023/A:1005040232597

McGuire, R. E., von Rosenvinge, T. T., & McDonald, F. B. 1986, ApJ, 301, 938, doi: 10.1086/163958

Ng, C. K., Reames, D. V., & Tylka, A. J. 2012, in American Institute of Physics Conference Series, Vol. 1436, Physics of the Heliosphere: A 10 Year Retrospective, ed. J. Heerikhuisen, G. Li, N. Pogorelov, & G. Zank, 212–218, doi: 10.1063/1.4723610

Ogilvie, K. W., Chornay, D. J., Fritzenreiter, R. J., et al. 1995, SSRv, 71, 55, doi: 10.1007/BF00751326

Owen, C. J., Balogh, A., Cowley, S. W. H., Richardson, I. G., & Tsurutani, B. T. 1991, Planet. Space Sci., 39, 761, doi: 10.1016/0032-0633(91)90071-H

Owen, C. J., Cowley, S. W. H., Richardson, I. G., & Balogh, A. 1990, Planet. Space Sci., 38, 851, doi: 10.1016/0032-0633(90)90054-T

Reames, D. V., Ng, C. K., & Berdichevsky, D. 2001, ApJ, 550, 1064, doi: 10.1086/319810

Richardson, I. G. 2018, Living Reviews in Solar Physics, 15, 1, doi: 10.1007/s41116-017-0011-z

Richardson, I. G., & Cane, H. V. 1995, JGR, 100, 23397, doi: 10.1029/95JA02684

—. 2010a, SoPh, 264, 189, doi: 10.1007/s11207-010-9568-6

—. 2010b, Journal of Geophysical Research (Space Physics), 115, A07103, doi: 10.1029/2009JA015039

Richardson, I. G., & Reames, D. V. 1993, ApJS, 85, 411, doi: 10.1086/191769

Sanderson, T. R., Reinhard, R., van Nes, P., & Wenzel, K. P. 1985, JGR, 90, 19, doi: 10.1029/JA090iA01p00019

Sarris, E. T., & van Allen, J. A. 1974, JGR, 79, 4157, doi: 10.1029/JA079i028p04157

Shen, C., Wang, Y., Ye, P., & Wang, S. 2008, SoPh, 252, 409, doi: 10.1007/s11207-008-9268-7

Smith, C. W., L'Heureux, J., Ness, N. F., et al. 1998, SSRv, 86, 613, doi: 10.1023/A:1005092216668

Szabo, A. 1994, JGR, 99, 14737, doi: 10.1029/94JA00782

Szabo, A., Smith, C. W., Paularena, K. I., & Skoug, R. M. 2001, in AGU Spring Meeting Abstracts, Vol. 2001, SH62A–06

Thomsen, M. F. 1985, Washington DC American Geophysical Union Geophysical Monograph Series, 35, 253, doi: 10.1029/GM035p0253

Tokar, R. L., Gary, S. P., Gosling, J. T., et al. 2000, JGR, 105, 7521, doi: 10.1029/1999JA000097

Trotta, D., Valentini, F., Burgess, D., & Servidio, S. 2021, Proceedings of the National Academy of Science, 118, 2026764118, doi: 10.1073/pnas.2026764118

Tsurutani, B. T., & Lin, R. P. 1985, JGR, 90, 1, doi: 10.1029/JA090iA01p00001

van Nes, P., Reinhard, R., Sanderson, T. R., Wenzel, K. P., & Zwickl, R. D. 1984, JGR, 89, 2122, doi: 10.1029/JA089iA04p02122

van Nes, P., Roelof, E. C., Reinhard, R., Sanderson, T. R., & Wenzel, K. P. 1985, JGR, 90, 3981, doi: 10.1029/JA090iA05p03981

Vinas, A. F., & Scudder, J. D. 1986, JGR, 91, 39, doi: 10.1029/JA091iA01p00039

Wenzel, K. P., Reinhard, R., Sanderson, T. R., & Sarris, E. T. 1985, JGR, 90, 12, doi: 10.1029/JA090iA01p00012

Wilson, L. B., I., Cattell, C. A., Kellogg, P. J., et al. 2009, Journal of Geophysical Research (Space Physics), 114, A10106, doi: 10.1029/2009JA014376

—. 2010, Journal of Geophysical Research (Space Physics), 115, A12104, doi: 10.1029/2010JA015332

Wilson, L. B., I., Koval, A., Szabo, A., et al. 2017, Journal of Geophysical Research (Space Physics), 122, 9115, doi: 10.1002/2017JA024352

Wilson, Lynn B., I., Brosius, A. L., Gopalswamy, N., et al. 2021, Reviews of Geophysics, 59, e2020RG000714, doi: 10.1029/2020RG000714

Wilson, L. B. 2016, Washington DC American Geophysical Union Geophysical Monograph Series, 216, 269, doi: 10.1002/9781119055006.ch16

Wilson, L. B., Koval, A., Szabo, A., et al. 2013, Journal of Geophysical Research (Space Physics), 118, 5, doi: 10.1029/2012JA018167

Yang, L., Berger, L., Wimmer-Schweingruber, R. F., et al. 2020, ApJL, 888, L22, doi: 10.3847/2041-8213/ab629d